This is a preprint of the following article, which is available from mdolab.engin.umich.edu
Gray, A. C., Kennedy, G. J. and Martins, J. R. R. A., Geometrically Nonlinear High-fidelity Aerostructural Optimization Including Geometric Design Variables, *AIAA Aviation Forum*, June 2023.
The original article may differ from this preprint and is available at
https://doi.org/10.2514/6.2023-3316.

Geometrically Nonlinear High-fidelity Aerostructural Optimization Including Geometric Design Variables

Alasdair C. Gray[1,*], Graeme J. Kennedy[2], and Joaquim R. R. A. Martins[1]
[1]*University of Michigan, Ann Arbor, MI, 48109*
[2]*Georgia Institute of Technology, Atlanta, GA, 30332*

Abstract

Over the past decade, advances in MDO have enabled the optimization of aircraft wings using high-fidelity simulations of their coupled aerodynamic and structural behavior. Using RANS CFD and detailed structural finite element wingbox models, the aerodynamic shape and internal structural sizing of a wing can be optimized concurrently to tailor the aeroelastic behavior of the wing and optimally trade-off drag and structural mass. This capability makes MDO a key enabling technology for the next generation of efficient high-aspect-ratio transport aircraft. However, as their aspect-ratios increase, these wings increasingly exhibit geometrically nonlinear behavior that cannot be correctly modeled by typical linear structural analysis methods. This paper builds on our previous work, demonstrating the first simultaneous optimization of a wing's aerodynamic shape and structural sizing using high-fidelity geometrically nonlinear models. Our methods are implemented in the open-source finite element library, TACS, and include a geometrically nonlinear shell element formulation, an efficient nonlinear solver, and a constitutive model for stiffened shells. We then demonstrate the ability to couple these nonlinear structural analysis tools to a high-fidelity RANS CFD solver using a geometrically nonlinear load and displacement transfer scheme. Finally we use this capability to perform a series of fuel-burn minimizations of a single-aisle commercial transport aircraft wing featuring 578 design variables and 1287 constraints. Our results suggest that geometrically nonlinear effects noticeably change the optimum trade-off between drag and structural mass at aspect-ratios typical of modern transport aircraft, even if the attained fuel-burn is similar.

1 Introduction

Aircraft manufacturers are constantly striving to design and build more efficient aircraft, be it for environmental reasons or purely financial ones. One of the conceptually simplest ways to increase the aerodynamic efficiency of aircraft is to increase the aspect-ratio of their wings. Consequently, the past five decades have seen a steady increase in the aspect-ratio of commercial aircraft wings.

Key to these increases has been the development of novel airframe technologies, such as advanced composite materials, passive load alleviation through aeroelastic tailoring of wing structures, and

[1]Corresponding author: alachris@umich.edu

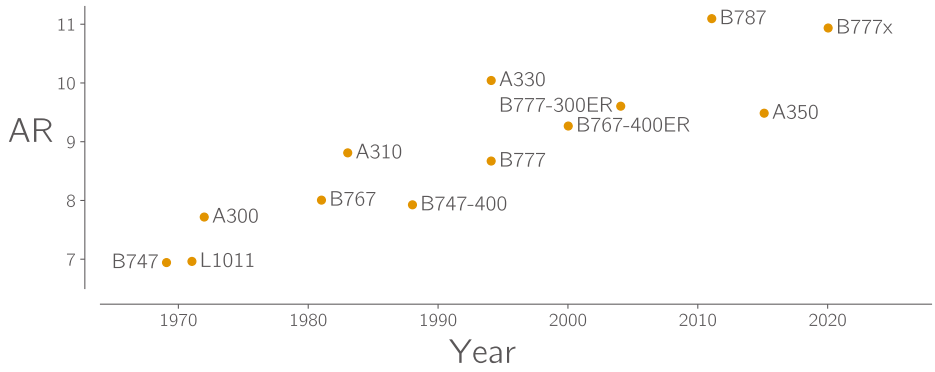

Figure 1: The aspect-ratio of commercial transport aircraft wings has increased 50% in the past 50 years [1].

active load alleviation through control laws. However, the integration of these technologies into modern airframes has itself been enabled by advances in the computational tools used to design them. As the aspect-ratio of wings increases, they naturally become more flexible, leading to a stronger coupling between their structural and aerodynamic behavior, requiring coupled analysis techniques. The increasing accessibility of tools such as NASTRAN early in the design cycle has enabled the aircraft industry to transition from viewing this aeroelastic coupling as a problem to be avoided, to an opportunity to be exploited.

Many of the key enabling technologies of high-aspect-ratio wing (HARW) mentioned above bring with them an increased number of design parameters, further complicating the already complex task of wing design. In response to this need, there has also been increased interest in the application of multidisciplinary design optimisation (MDO) methods to aircraft design and, in particular, aerostructural wing design [2–5].

Due to the replacement of engineering intuition with simulation results, the computational methods used in MDO frameworks must be capable of modeling the physical phenomena that limit the design space in reality. If not, there is a common tendency for the optimizers to take advantage of gaps in the modeled physics, producing unrealistic optimal designs. HARW exhibit geometrically nonlinear behavior, as a result of their high flexibility, that cannot be correctly modeled using linear finite element (FE) methods. Using linear models may lead to inaccurate sizing of wing structures, both due to the direct inaccuracy in the linear stress calculation and inaccuracy in the deflected wing shape that consequently affects the aerodynamic load distribution over the wing. Examples of such geometrically nonlinear behavior include Brazier loading, large compressive rib loads not captured by linear models [6–8], and the nonlinear coupling of chordwise bending and torsion, which can lead to significant changes in static trim [9, 10] and flutter onset [11].

Geometrically nonlinear FE methods for structural analysis are a mature technology available in most commercial structural analysis codes and have been incorporated into several aeroelastic analysis frameworks in the past two decades [9, 10, 12–23]. Table 1 presents a summary of works, which have pushed the state of the art in terms of either fidelity or geometric nonlinearity in aeroelastic analysis and optimization. A subset of this work has included aeroelastic optimization using geometrically nonlinear models. The PROTEUS framework, developed by Werter and De Breuker [28], and UM/NAST, developed by Cesnik et al [47], have both been used to perform geometrically nonlinear aeroelastic optimization including flutter [22], gust-load [31] and fatigue-life constraints [32].

Although these tools have been used to optimize wing structures based on geometrically nonlinear

Table 1: Summary of the literature on high-fidelity and geometrically nonlinear aeroelasticity.

Author/Tool	Aerodynamic Model[1,2]	Structural Model[2,3]	Optimisation Variables		
			Structure	Planform	Shape
Howcroft et al. [9]	VLM/DLM	NL Beam			
Garcia [10], Bartels et al. [18]	RANS	NL Beam			
Verri et al. [24]	RANS	NL Shell			
Zimmer et al. [25]	RANS	NL Shell			
Calderon et al. [26, 27]	VLM	NL Beam	✓		
PROTEUS [28–34]	VLM	NL Beam	✓		
Jovanov [35]	Euler	NL Beam	✓		
Stanford et al. [7, 36–40]	VLM	Shell	✓		
Stanford [41]	VLM	Shell	✓	✓	✓
UM/NAST [22]	ST	NL Beam	✓	✓	
Dillinger et al. [42]	Euler	Shell	✓		
MACH [5, 43–46]	RANS	Shell	✓	✓	✓
Gray and Martins [8]	RANS	NL Shell	✓		
This work	RANS	NL Shell	✓	✓	✓

[1] Aerodynamic models: doublet lattice method (DLM) = Doublet lattice method, vortex lattice method (VLM) = Vortex lattice method, ST = Strip theory, Q3D = Quasi 3D, Euler = Euler computational fluid dynamics (CFD), RANS = RANS CFD

[2] Fidelity: Low, Mid, High

[3] Structural models: NL = Nonlinear

aeroelastic analysis, few works have explicitly investigated the differences in wing designs optimized with and without considering such effects. These implications were studied in two papers by Calderon et al. [26, 27], using the low-fidelity aeroelastic framework NeoCASS [15]. The results of the work found that wings sized using geometrically nonlinear structural analysis were lighter over the entire range of aspect ratios studied, had roughly equal aerodynamic efficiency, and had a higher optimum aspect ratio than those optimized based on linear structural analysis.

However, all of these works use low-fidelity beam FE models, and often low-fidelity panel-based aerodynamic models. While beam models are suitable for modeling the global structural dynamics of slender wings, they cannot accurately predict localized stress distributions in the wingbox. Similarly, potential flow models can accurately predict aerodynamic load distributions in subsonic conditions, but miss the viscous and compressible flow effects required to accurately predict cruise drag. Most aerostructural optimization problems involve trading off structural weight, peak stress levels, and cruise drag, thus requiring models that can accurately predict these quantities. These accurate predictions can only be achieved using detailed structural FE models coupled to aerodynamic models that capture viscous and compressible flow effects, such as Reynolds-averaged Navier-Stokes (RANS) CFD [2, 4]. Additionally, RANS CFD can remove spurious multimodality in the design space that can appear when using lower fidelity inviscid methods [48].

The coupling of RANS CFD with nonlinear shell FE models represents the current state of the art in high-fidelity geometrically nonlinear aeroelastic modeling. Stickan et al. [49], Zimmer et al. [25], and Verri et al. [24] demonstrated this capability, by coupling TAU and Abaqus at Airbus, TAU and NASTRAN at DLR, and CFD++ and NASTRAN at Embraer, respectively. These works showed that geometrically nonlinear effects are visible in wings with aspect-ratios typical of the latest generation

of commercial transport aircraft.

In previous work, we incorporated geometrically nonlinear shell elements into the MACH framework to enable geometrically nonlinear coupled analysis and optimization using RANS CFD and shell FE models [8]. Using this framework, we demonstrated the first detailed wingbox sizing optimization using coupled high-fidelity RANS CFD and geometrically nonlinear shell finite element models. However, this work was subject to two limitations:

1. The load and displacement transfer scheme was not geometrically exact, in that it used linear rotation terms when transferring displacements, and computes transferred loads in the undeformed configuration.
2. Derivatives with respect to node coordinates were not available for the nonlinear shell elements, meaning only the structural sizing of the wing was optimized, while the geometry remained fixed.

In this work, we eliminate these two shortcomings, and demonstrate the first high-fidelity aerostructural optimization that is fully geometrically nonlinear and includes both structural and geometric design variables. In doing so, we aim to investigate how geometrically nonlinear aeroelastic effects affect the optimal design of HARW.

The remainder of the paper is organized as follows: Section 2 describes our nonlinear structural analysis capabilities, including the nonlinear shell element formulation, nonlinear solver, and stiffened shell constitutive model. Section 3 covers the coupling of the structural analysis with RANS CFD, including the load-displacement transfer scheme. Finally, Section 4 demonstrates the capabilities of these tools by performing aerostructural optimization studies on a single-aisle commercial transport aircraft wing.

2 Geometrically Nonlinear Structural Analysis

For structural analysis, we use TACS (toolkit for analysis of composite structures)[1] [50], an efficient parallel FE library that is particularly effective at solving the poorly conditioned systems of equations that result from the thin-walled structures typical of airframes. TACS uses a fully analytic adjoint implementation to compute derivatives of functions of interest such as aggregated stress constraints efficiently with respect to large numbers of design variables. The version of TACS used in our previous work with MACH was an older version of the code which featured a different nonlinear element implementation that could not compute geometric derivatives. In this work, we use the latest, open-source version of the code.

2.1 Nonlinear Shell Elements

The nonlinear shell elements in TACS utilize a mixed interpolation of tensorial components (MITC) formulation for the out-of-plane shear and in-plane normal strain components that are susceptible to shear or membrane locking [51, 52]. The shell elements implement a nonlinear drilling penalization term that is designed to ensure consistency between the in-plane rotation and rotation about the shell normal [53, 54]. The shell formulation utilizes all linear and nonlinear contributions to the Green strain for the in-plane, bending and shear strain components. A director field formulation is used to parameterize the rate-of-change of the displacements through the thickness of the shell [55, 56]. The director field is computed using a quadratic approximation of a rotation matrix applied to the shell unit normal, where the matrix is computed using the degrees of freedom at each node. Given the rotational

[1] github.com/smdogroup/tacs

degrees of freedom $\theta \in \mathbb{R}^3$, the quadratic approximation of the rotation matrix $\mathbf{C}$ is computed using the skew-symmetric cross-product matrix $\theta^\times$:

$$\mathbf{C}(\theta) = \mathbf{I} + \theta^\times + \frac{1}{2}\theta^\times\theta^\times = (1 - \frac{1}{2}\theta^T\theta)\mathbf{I} + \theta^\times + \frac{1}{2}\theta\theta^T \approx \mathbf{C}_{\text{exact}}(\theta) = \exp(\theta^\times) = \sum_{k=0}^{\infty} \frac{1}{k!}\left(\theta^\times\right)^k \quad (1)$$

This quadratic approximation of the exponential map enables modeling of near extension-free moderate rotations. This capability is important for flexible high-aspect ratio transport aircraft wings that experience large tip deflections and moderate rotations. The rate-of-change of displacement through the shell thickness is computed from the rotation (1) as

$$\mathbf{d} = (\mathbf{C}(\theta) - \mathbf{I})\hat{\mathbf{n}} \quad (2)$$

where $\hat{\mathbf{n}}$ is the shell surface normal and $\mathbf{d}$ is the rate of change of deformation through the thickness. The deformation (2) is interpolated across the element from the nodes using standard Largrange interpolation and is used to compute the in-plane and bending strains.

2.2 Nonlinear Solver

To solve geometrically nonlinear structural problems in TACS we implement a Newton–Raphson based solver, which contains a small number of improvements on the solver used in our previous work [8]. In nonlinear structural problems we solve for equilibrium in the derformed rather than undeformed configuration, as a result the equilibrium can no longer be written as a linear system $\mathbf{Ku} = \mathbf{f}$ but should instead be written as a system of nonlinear residual equations.

$$\mathbf{r}(\mathbf{u}) = \mathbf{F}_{\text{in}}(\mathbf{u}) + \mathbf{F}_{\text{ex}}(\mathbf{u}) = 0 \quad (3)$$

Where $\mathbf{u}$ are the nodal displacements, $\mathbf{F}_{\text{in}}$ are the internal forces resulting from stresses in the structure, and $\mathbf{F}_{\text{ex}}$ are the externally applied forces. As in our previous work, this solver uses adaptive load-incrementation/continuation, meaning the solver is repeatedly called on a modified set of residual equations where the external forces are scaled down by a load factor λ:

$$\mathbf{r}(\mathbf{u}, \lambda) = \mathbf{F}_{\text{in}}(\mathbf{u}) + \lambda\mathbf{F}_{\text{ex}}(\mathbf{u}) = 0 \quad (4)$$

Using the Newton–Raphson method, we can solve these equations by repeatedly computing a displacement update using the tangent stiffness matrix, $\mathbf{K}_\mathrm{T}$, a local linearization of the nonlinear residual equations:

$$\mathbf{K}_\mathrm{T}(\mathbf{u}_\mathrm{i}, \lambda) = \frac{\partial \mathbf{r}}{\partial \mathbf{u}}|_{u=u_i} = \frac{\partial \mathbf{F}_{\text{in}}}{\partial \mathbf{u}}\Big|_{u=u_i} + \lambda\frac{\partial \mathbf{F}_{\text{ex}}}{\partial \mathbf{u}}\Big|_{u=u_i} \quad (5)$$

$$\mathbf{\Delta u}_\mathrm{i} = -\mathbf{K}_\mathrm{T}(\mathbf{u}_\mathrm{i}, \lambda)^{-1}\mathbf{r}(\mathbf{u}_\mathrm{i}, \lambda) \quad (6)$$

The solution of this system for a given load factor is a point on the equilibrium path of the structure, $\mathbf{u}^*(\lambda)$. To control the size of each load increment, we use the adaptive load stepping method of Beluni and Chulya [57], where the current load step is increased or decreased based on the actual and desired number of iterations taken to solve the previous increment:

$$\lambda_j - \lambda_{j-1} = \Delta\lambda_j = \sqrt{\frac{N_{des}}{N_{j-1}}}\Delta\lambda_{j-1} \quad (7)$$

The desired number of iterations, N_{des}, can then be used to control how ambitious the solver should be with its load incrementation.

Previously, the nonlinear solve for each load increment started from the equilibrium point found in the previous increment, $\mathbf{u}_{0,j} = \mathbf{u}^*_{j-1}$. In our new implementation, we keep track of the last n discovered equilibrium points and use them to extrapolate the next point on the equilibrium path, which is then used as the initial guess for the next Newton–Raphson solve. This reduces the number of iterations required to reach convergence due to the Newton–Raphson method's sensitivity to the quality of its starting point. Using Lagrange polynomial interpolation, the extrapolated equilibrium point is given by a linear combination of the previous points, making the extrapolation operation very cheap:

$$\mathbf{u}_{0,j} = \sum_{i=0}^{n-1} \mathbf{u}^*_i \prod_{k=0, k\neq i}^{n-1} \frac{\lambda_j - \lambda_k}{\lambda_i - \lambda_k} \tag{8}$$

This approach can be considered a predictor-corrector continuation method, where the equilibrium path extrapolation is the predictor stage and the Newton–Raphson solve is the corrector stage.

Our second improvement over our previous implementation is the use of adaptive linear convergence. Due to the extremely poor conditioning of shell structural models, TACS solves the linear system in Equation (6) using GMRES preconditioned by a complete LU factorization. This means that the most expensive operation in the solver is recomputing the linear system preconditioner. Therefore, during each Newton–Raphson solution, we update the tangent stiffness matrix every iteration but only recompute the preconditioner if the previous linear solve took more than a specified number of iterations to converge. In combination with this we use the variant of the Eisenstat–Walker method proposed by An et al. [58] to adapt the tolerance to which the linear system is solved. This method avoids "over–solving" the linear system early in the Newton–Raphson solve and tightens the convergence tolerance as the nonlinear solver approaches a solution. These two appraches are complementary since it is generally not possible to solve the linear system tightly with an out-of-date preconditioner, while updating the preconditioner every iteration generally results in very tight linear convergence in only 1-2 GMRES iterations. Figure 2 demonstrates the effectiveness of this approach on the geometrically nonlinear hemispherical shell benchmark problem described by Sze et al. [59][2]. The plots show the nonlinear (top) and linear (bottom) residual from each Newton–Raphson iteration during the solve. Although using adaptive linear convergence requires more Newton–Raphson iterations to converge, the time to reach the solution is reduced by over 35% due to the reduced number of LU factorizations required.

Finally, we retain the use of the novel minimum energy restart method for our load continuation scheme [8]. This method is used to compute the load factor to start at when restarting the continuation from a previous solution by computing the load factor that minimizes the work done in the resulting Newton–Raphson step:

$$\lambda^* = \frac{-\left(\boldsymbol{\Delta u}_{\mathrm{i}}{}^{\mathsf{T}} \mathbf{F}_{\mathrm{ex}} + \boldsymbol{\Delta u}_{\mathrm{e}}{}^{\mathsf{T}} \mathbf{F}_{\mathrm{in}}\right)}{2\boldsymbol{\Delta u}_{\mathrm{e}}{}^{\mathsf{T}} \mathbf{F}_{\mathrm{ex}}}, \quad \boldsymbol{\Delta u}_{\mathrm{i}} = \mathbf{K}_{\mathsf{T}}{}^{-1} \mathbf{F}_{\mathrm{in}}, \ \boldsymbol{\Delta u}_{\mathrm{e}} = \mathbf{K}_{\mathsf{T}}{}^{-1} \mathbf{F}_{\mathrm{ex}} \tag{9}$$

This technique is particularly useful during optimization where the same analysis may be repeated 1000's of times with slightly modified external loads and structural sizing parameters.

[2] The mesh used in this case was significantly finer than the 16x16 mesh shown in the referenced manuscript.

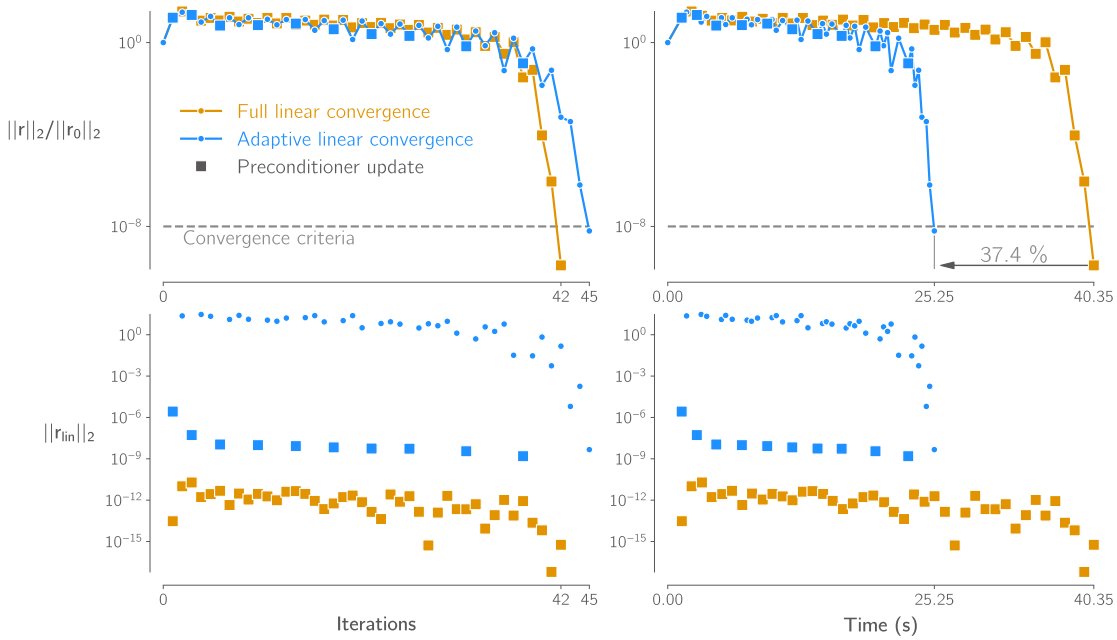

Figure 2: Using adaptive linear convergence speeds up the nonlinear solver, in this case by over 35%.

2.3 Stiffened Shell Constitutive Model

Practical optimization aerospace structures requires the ability to model stiffened shells. In this work, rather than modeling stiffeners explicitly, we use a smeared stiffener approach where the stiffness of the stiffener is smeared over the shell. This approach is advantageous for optimization applications because it allows the stiffener geometry and layout to be optimized without the need to modify the structural mesh. This constitutive model is based on the theory described by Nemeth [60] and assumes the arrangement shown in Figure 3, stiffeners are modeled as beams aligned with the local coordinate system of the shell, with a uniform pitch, P_{stiff} and their centroids a distance Z_c from the shell mid-plane.

Using first order shear deformation theory[3] the stress-strain relations for the shell are:

$$\begin{bmatrix} N_1 \\ N_2 \\ N_{12} \end{bmatrix} = \begin{bmatrix} A_{11} & A_{12} & A_{16} \\ A_{12} & A_{22} & A_{26} \\ A_{13} & A_{26} & A_{66} \end{bmatrix} \begin{bmatrix} \epsilon_1^0 \\ \epsilon_2^0 \\ \epsilon_{12}^0 \end{bmatrix} + \begin{bmatrix} B_{11} & B_{12} & B_{16} \\ B_{12} & B_{22} & B_{26} \\ B_{13} & B_{26} & B_{66} \end{bmatrix} \begin{bmatrix} \kappa_1 \\ \kappa_2 \\ \kappa_{12} \end{bmatrix} \tag{10}$$

$$\begin{bmatrix} M_1 \\ M_2 \\ M_{12} \end{bmatrix} = \begin{bmatrix} B_{11} & B_{12} & B_{16} \\ B_{12} & B_{22} & B_{26} \\ B_{13} & B_{26} & B_{66} \end{bmatrix} \begin{bmatrix} \epsilon_1^0 \\ \epsilon_2^0 \\ \epsilon_{12}^0 \end{bmatrix} + \begin{bmatrix} D_{11} & D_{12} & D_{16} \\ D_{12} & D_{22} & D_{26} \\ D_{13} & D_{26} & D_{66} \end{bmatrix} \begin{bmatrix} \kappa_1 \\ \kappa_2 \\ \kappa_{12} \end{bmatrix} \tag{11}$$

$$\begin{bmatrix} Q_2 \\ Q_1 \end{bmatrix} = \begin{bmatrix} A_{44} & A_{45} \\ A_{45} & A_{55} \end{bmatrix} \begin{bmatrix} \epsilon_{23}^0 \\ \epsilon_{13}^0 \end{bmatrix} \tag{12}$$

[3] also known as Uflyand–Mindlin plate theory for shells and Timoshenko theory for beams [61]

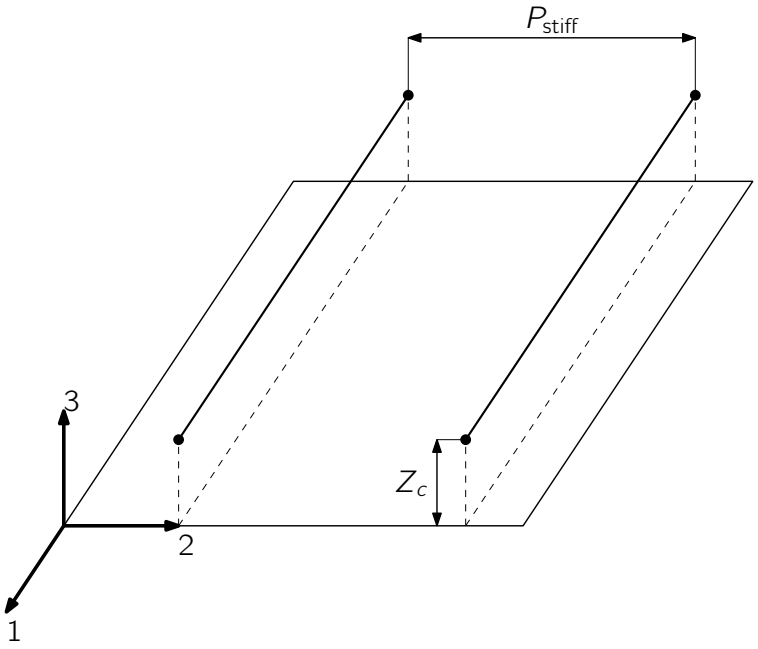

Figure 3: A stiffened shell panel with evenly spaced parallel stiffeners simplified to a 1D beam representation.

And for the beam:

$$\begin{bmatrix} F_1 \\ M_1 \\ M_2 \\ M_3 \\ V_{13} \\ V_{12} \end{bmatrix} = \begin{bmatrix} C_{11} & C_{12} & C_{13} & C_{14} & C_{15} & C_{16} \\ C_{12} & C_{22} & C_{23} & C_{24} & C_{25} & C_{26} \\ C_{13} & C_{23} & C_{33} & C_{34} & C_{35} & C_{36} \\ C_{14} & C_{24} & C_{34} & C_{44} & C_{45} & C_{46} \\ C_{15} & C_{25} & C_{35} & C_{45} & C_{55} & C_{56} \\ C_{16} & C_{26} & C_{36} & C_{46} & C_{56} & C_{66} \end{bmatrix} \begin{bmatrix} \epsilon_{11} \\ \chi_1 \\ \chi_2 \\ \chi_3 \\ \epsilon_{13} \\ \epsilon_{12} \end{bmatrix} \tag{13}$$

The strains at the stiffener centroid are computed by assuming that the linear variation in the strain assumed through the thickness of the shell continues up to the centroid of the stiffener. The stiffener centroid strains can then be calculated from the shell mid-plane strains using a strain transformation matrix $\mathbf{T}_\epsilon$:

$$\boldsymbol{\epsilon}_{\text{stiff}} = \mathbf{T}_\epsilon \boldsymbol{\epsilon}_{\text{shell}} \Rightarrow \begin{bmatrix} \epsilon_{11} \\ \chi_1 \\ \chi_2 \\ \chi_3 \\ \epsilon_{13} \\ \epsilon_{12} \end{bmatrix} = \begin{bmatrix} 1 & 0 & 0 & Z_c & 0 & 0 & 0 & 0 \\ 0 & 0 & 0 & 0 & 0 & -1/2 & 0 & 0 \\ 0 & 0 & 0 & 1 & 0 & 0 & 0 & 0 \\ 0 & 0 & 0 & 0 & 0 & 0 & 0 & 0 \\ 0 & 0 & 0 & 0 & 0 & 0 & 0 & 1 \\ 0 & 0 & 1/2 & 0 & 0 & Z_c/2 & 0 & 0 \end{bmatrix} \begin{bmatrix} \epsilon_1^0 \\ \epsilon_2^0 \\ \epsilon_{12}^0 \\ \kappa_1 \\ \kappa_2 \\ \kappa_{12} \\ \epsilon_{23}^0 \\ \epsilon_{13}^0 \end{bmatrix} \tag{14}$$

The loads felt at the shell mid-plane due to the stresses in the stiffener can be calculated using the reverse transformation and accounting for the stiffener pitch to smear the stiffener's stress contribution across the shell, resulting in the combined stress strain relationship:

$$\boldsymbol{\sigma} = \boldsymbol{\sigma}_{\text{shell}} + \frac{1}{P_{\text{stiff}}} \mathbf{T}_\epsilon^\top \boldsymbol{\sigma}_{\text{stiff}} = \boldsymbol{\sigma}_{\text{shell}} + \frac{1}{P_{\text{stiff}}} \mathbf{T}_\epsilon^\top \mathbf{C}_{\text{stiff}} \boldsymbol{\epsilon}_{\text{stiff}} \tag{15}$$

Combining Equations (14) and (15) gives the combined stiffness matrix:

$$\mathbf{C} = \mathbf{C}_{\text{shell}} + \frac{1}{P_{\text{stiff}}} \mathbf{T}_{\epsilon}^{\mathsf{T}} \mathbf{C}_{\text{stiff}} \mathbf{T}_{\epsilon} \tag{16}$$

Both the shell and the stiffener are modeled as smeared laminates. This approach parameterises a laminate by a collection of ply angles, θ_i, ply fractions, f_i, and an overall thickness, t. The laminate stiffness matrices are then a weighted sum of the stiffness matrices of each ply:

$$\mathbf{Q} = \sum_{i=1}^{N} f_i \bar{\mathbf{Q}}(\theta_i), \quad \mathbf{A} = t\mathbf{Q}, \quad \mathbf{B} = \mathbf{0}, \quad \mathbf{D} = \frac{t^3}{12}\mathbf{Q} \tag{17}$$

This approach is valid for thick laminates where the distribution of ply angles through the thickness is approximately uniform. Most importantly, the parameterisation avoids the discontinuities inherent in discrete laminate stacking sequences [62].

In this work, we assume the stiffener is laid-up symmetrically across the stiffener cross-section and the beam stiffness matrix therefore contains no coupling terms. The stiffener's stiffness can then be computed using the following effective modulii:

$$E_{\text{stiff}} = E_{11,\text{stiff}} = Q_{11} - \frac{Q_{12}^2}{Q_{22}}, \quad G_{\text{stiff}} = G_{12,\text{stiff}} = G_{13,\text{stiff}} = Q_{66} \tag{18}$$

and the resulting overall stiffness matrix for the stiffened shell is:

$$\mathbf{C} = \begin{bmatrix} \mathbf{A} & \mathbf{B} & \mathbf{0} \\ \mathbf{B} & \mathbf{D} & \mathbf{0} \\ \mathbf{0} & \mathbf{0} & \mathbf{A}_s \end{bmatrix} \tag{19}$$

$$\mathbf{A} = \mathbf{A}_{\text{shell}} + \frac{1}{P_{\text{stiff}}} \begin{bmatrix} A_{\text{stiff}} E_{\text{stiff}} & 0 & 0 \\ 0 & 0 & 0 \\ 0 & 0 & \frac{k G_{\text{stiff}} A_{\text{stiff}}}{4} \end{bmatrix} \tag{20}$$

$$\mathbf{B} = \mathbf{B}_{\text{shell}} + \frac{1}{P_{\text{stiff}}} \begin{bmatrix} A_{\text{stiff}} E_{\text{stiff}} Z_c & 0 & 0 \\ 0 & 0 & 0 \\ 0 & 0 & \frac{k G_{\text{stiff}} A_{\text{stiff}} Z_c}{4} \end{bmatrix} \tag{21}$$

$$\mathbf{D} = \mathbf{D}_{\text{shell}} + \frac{1}{P_{\text{stiff}}} \begin{bmatrix} E_{\text{stiff}}(I_{33,\text{stiff}} + A_{\text{stiff}} Z_c^2) & 0 & 0 \\ 0 & 0 & 0 \\ 0 & 0 & \frac{G_{\text{stiff}}(J_{\text{stiff}} + k A_{\text{stiff}} Z_c^2)}{4} \end{bmatrix} \tag{22}$$

where A_{stiff} is the area, $I_{33,\text{stiff}}$ the second moment of area and J_{stiff} the polar moment of inertia of the stiffener cross-section about its centroid. k is the shear correction factor. This formulation is similar to that used in TACS previously [43, 45], except for the additional B_{66} and D_{66} terms.

2.4 Failure Criteria

We predict material failure in the stiffened shell using the the Tsai–Wu failure criterion [63]:

$$FI = F_1\sigma_{11} + F_2\sigma_{22} + F_{11}\sigma_{11}^2 + F_{22}\sigma_{22}^2 + F_{66}\sigma_{12}^2 + F_{12}\sigma_{11}\sigma_{22} = \boldsymbol{\sigma}^{\mathsf{T}}\mathbf{F}\boldsymbol{\sigma} + \mathbf{f}^{\mathsf{T}}\boldsymbol{\sigma} \tag{23}$$

Where F_{11} F_{22}, F_{66} and F_{12} capture the material strengths under axial, shear and bi-axial loading, and F_1 and F_2 capture any differences between the strengths in tension and compression. This criteria

has the disadvantage that the failure value does not scale linearly with the stresses and thus applying a safety factor to a failure constraint during optimisation is not a valid approach. In other words, constraining the structure to have a maximum failure value of 1/2 does not mean the structure has a factor of safety of 2, since $FI(a\boldsymbol{\sigma}) \neq aFI(\boldsymbol{\sigma})$.

Unlike the von-Mises criteria for isotropic materials, using the square root of Equation (23) is not possible because it contains both quadratic and linear terms and can sometimes be negative. Instead we compute the strength ratio, the factor by which the stresses would need to be scaled down to be at the failure boundary:

$$SR = \alpha, \quad s.t. \left(\frac{1}{\alpha}\boldsymbol{\sigma}\right)^T \mathbf{F} \left(\frac{1}{\alpha}\boldsymbol{\sigma}\right) + \mathbf{f}^\mathsf{T} \left(\frac{1}{\alpha}\boldsymbol{\sigma}\right) = 1 \tag{24}$$

This equation has the roots

$$\alpha = 1/2 \left(\mathbf{f}^\mathsf{T}\boldsymbol{\sigma} \pm \sqrt{(\mathbf{f}^\mathsf{T}\boldsymbol{\sigma})^2 + 4\boldsymbol{\sigma}^T\mathbf{F}\boldsymbol{\sigma}}\right) \tag{25}$$

Since the Tsai-Wu criterion is only physically valid if the F matrix is positive definite, the strength ratio is:

$$SR = 1/2 \left(\mathbf{f}^\mathsf{T}\boldsymbol{\sigma} + \sqrt{(\mathbf{f}^\mathsf{T}\boldsymbol{\sigma})^2 + 4\boldsymbol{\sigma}^T\mathbf{F}\boldsymbol{\sigma}}\right) \tag{26}$$

We compute this strength ratio at the top and bottom surfaces of the panel, the tip of the stiffener, and for each ply angle at each location.

Buckling is a critical failure mode for the thin shell structures in aircraft and thus optimising a wingbox without constraints on buckling failure is unlikely to produce realistic designs. When using geometrically nonlinear shell models, buckling poses an additional problem since the finite element model itself may buckle, which would almost certainly result in failure to converge the coupled aeroelastic analysis. For these reasons, we compute a force-based buckling failure criteria in each element. We use the combined axial and shear buckling failure envelope described by Stroud and Agranoff [64], converted to a strength ratio in the same way as the Tsai-Wu failure criteria above to ensure that constraints applied during optimization can enforce a desired buckling margin:

$$SR = 1/2 \left(\frac{N_1}{N_{1,\text{crit}}} + \sqrt{\left(\frac{N_1}{N_{1,\text{crit}}}\right)^2 + 4\left(\frac{N_{12}}{N_{12,\text{crit}}}\right)^2}\right) \tag{27}$$

This buckling criteria is computed both for global buckling of the stiffened shell, and for local buckling of the panel between stiffeners [43, 45]. These two buckling strength ratios are combined with the Tsai-Wu strength ratios using KS aggregation [65] to produce a single value for each element.

3 Aerostructural Coupling and Derivative Computation

To enable coupled analysis and optimization using the capabilities described above, we use the MPhys[4] library, which is built on-top of OpenMDAO[5] [66]. OpenMDAO is an open-source Python tool that greatly simplifies the process of building and running complex multidisciplinary computational models. The tool allows users to define coupled models as a series of "components" and the connections

[4] github.com/OpenMDAO/MPhys
[5] github.com/OpenMDAO/openmdao

between their inputs and outputs. OpenMDAO then automatically coordinates the execution of these components to both solve coupled analyses and, crucially for optimization, compute coupled derivatives, regardless of the number and arrangement of components in the model [67]. MPhys is a library developed to standardize the use and coupling of high-fidelity CFD, FE, and other physics codes in OpenMDAO. MPhys aims to allow users to quickly build and run complex multidisciplinary models, and to easily swap in and out different codes fidelities for a given discipline without any substantial changes to the setup of their models. MPhys has already been used in published work for high-fidelity aeropropulsive [68], aerothermal [69] and aerostructural optimization [70, 71] optimization using a variety of codes. TACS, along with the computational tools described below have existing MPhys interfaces that we use in this work.

3.1 Aerodynamic Analysis

For aerodynamic analysis, we use ADflow[6], a finite-volume CFD solver for structured multiblock and overset meshes [72]. ADflow solves the compressible Euler, laminar Navier–Stokes, and RANS equations with a second-order accurate spatial discretization. In this work, we solve the RANS equations with the Spalart–Allmaras turbulence model. The solver employs a variety of numerical methods to converge to a steady-state solution robustly and efficiently, including multigrid, approximate Newton-Krylov, and Newton-Krylov algorithms [73]. The combination of these various iterative methods makes ADflow robust and fast. ADflow also solves the discrete adjoint equations, enabling efficient computation of derivatives independent of the number of design variables. The solution of the discrete adjoint in ADflow relies on the ADjoint approach, which uses algorithmic differentiation (AD) to compute partial derivatives and a Krylov method to solve the linear system [74].

3.2 Geometrically Nonlinear Load and Displacement Transfer

To transfer loads and displacements between the CFD and FE models, we use MELD (matching-based extrapolation of loads and displacements), which is a part of the FUNtoFEM framework[7] [75]. MELD transfers displacements from the structural mesh to the aerodynamic mesh by by linking each aerodynamic surface node to a fixed number of nearest structural nodes. The displacement of each aerodynamic surface node is computed by finding an optimal rigid rotation and translation that are computed from the displacements of the set of linked structural nodes [76]. The use of a rigid rotation matrix makes MELD's displacement transfer geometrically exact. In contrast, the RLT (rigid link transfer) scheme used in our previous work relies on a linear rotation approximation when extrapolating displacements to aerodynamic nodes that are not coincident with the structural mesh, as shown in Figure 4.

3.3 Geometry Parameterization

To parameterize the geometry of our aerodynamic and structural models during optimizations, we use pyGeo[8], in particular, its free-form deformation (FFD) implementation. This approach embeds the mesh nodes of a model in a volume defined by a set of control points. Deformations at the control points are then smoothly mapped to the embedded points using spline-based interpolation. In this way, point sets from multiple models are deformed consistently, which is critical in the case of aerostructural optimization where the aerodynamic and structural geometries should remain coincident

[6] github.com/mdolab/adflow
[7] github.com/smdogroup/funtofem
[8] github.com/mdolab/pygeo

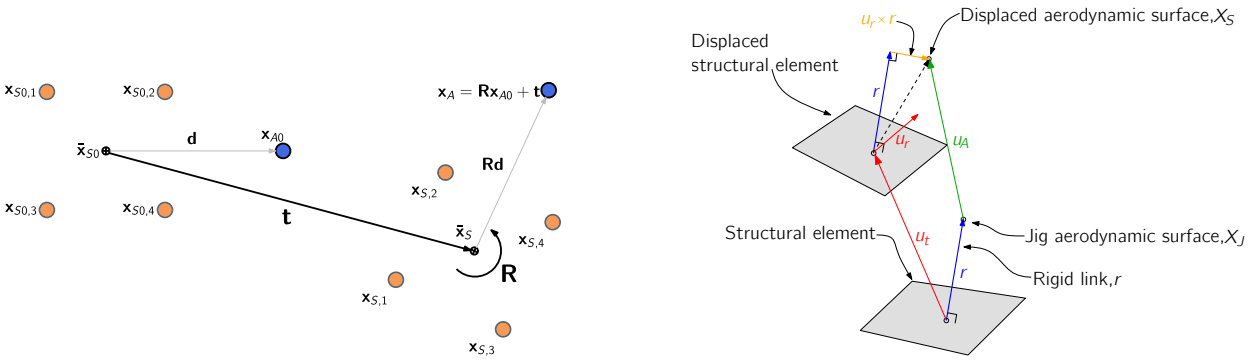

(a) MELD [76]. (b) RLT [5].

Figure 4: MELD uses a geometrically exact rotation term when transferring displacements, while RLT uses a linearized approximation, $u_r \times r$.

as they change. The derivatives of the embedded points' coordinates with respect to user-defined design variables that dictate the control point deformations can be computed quickly and accurately because the mapping is analytic [77].

3.4 Coupled Solvers

MPhys allows coupled models to be solved using any of the linear and nonlinear solvers available in OpenMDAO. For primal aerostructural analyses, we use a nonlinear block Gauss–Seidel approach, which is a partitioned approach commonly used for solving coupled aerostructural problems [5, 8][78, Sec. 13.2.5]. In each cycle of the nonlinear solution, the structural model is converged tightly, while the aerodynamic model is only converged loosely. The solver is also stabilized using Aitken acceleration [79]. For the coupled adjoint solution, we use the FGMRES iterative solver [80] to converge the monolithic coupled linear system. Each iteration of FGMRES is preconditioned with one round of linear block Gauss–Seidel, which involves approximately solving the single discipline adjoints in TACS and ADflow.

3.5 Optimizer

To perform our optimizations, we use the sparse nonlinear optimizer, SNOPT [81], a high-performance sequential quadratic programming (SQP) optimizer that has proven to excel at the large-scale, sparse, constrained nonlinear optimization problems typical of high-fidelity MDO [82]. OpenMDAO interfaces with SNOPT through pyOptSparse[9] [83], an object-oriented framework that provides a general interface to many optimizers and greatly simplifies the task of defining large sparse Jacobians that are crucial for the performance of large-scale optimizers like SNOPT.

4 Aerostructural Optimization Studies

This section covers the aircraft model and problem formulation used in our optimization studies. The goal of these studies is not only to demonstrate the capabilities described in Section 2, but also to investigate how significant the impact of geometric nonlinearity is on the design of wings with aspect-ratios that may be seen in the coming generations of commercial transport aircraft.

[9] https://github.com/mdolab/pyoptsparse

4.1 Aircraft Model

The baseline wing model for our optimizations is a model known as the MACH tutorial wing. This model is available in the public MPhys repository and has already been used for aerostructural optimization by other researchers integrating their tools into MPhys [84]. The geometry (shown in Figure 5) consists of a single wing whose planform is based on the Boeing 717, with a uniform, untwisted RAE2822 cross-section. Tables 2 and 3 list information about the aircraft and the flight conditions used in our optimization studies, which are all based on publicly available data for the Boeing 717.

The wing contains a conformal wingbox with upper and lower skins, leading and trailing edge spars, and 23 ribs[10]. The outboard section of the wingbox extends from 15 to 65 % of the chord. A side-of-body junction is modeled at a semispan of 1.5m, inboard of which the wingbox is unswept, resembling a center-box. The wingbox is subject to symmetry conditions at the centerline and is fixed in the chordwise and vertical directions at the side-of-body junction as shown in Figure 5.

The wingbox panels are modeled as composites using the ply properties shown in Table 4, taken from Brooks et al. [2]. Both the shell and stiffeners in every panel of the wingbox are assumed to consist of a [0, -45, +45, 90]° layup. We use different layups of these plies for different components in the wingbox based on values used by Dillinger [85]. In the upper and lower skin shells and in all stiffeners, we assume a 0° biased layup with ply fractions of [44.41%, 22.2%, 22.2%, 11.19%], while in the spar and rib shells we use a more isotropic [10%, 20%, 35%, 35%]. In the skins, the stiffeners and 0° plies are aligned with the trailing edge spar, in the spars and ribs they are vertically oriented.

Table 2: Boeing 717 specifications assumed in this work

	Quantity	Description	Value
Masses			
	M_{payload}	Payload mass	14.5×10^3 kg
	M_{frame}	Operating empty mass (minus wing)	25×10^3 kg[a]
	$M_{\text{fuel, res}}$	Reserve fuel mass	2×10^3 kg
Baseline wing geometry			
	b	Semispan	14 m
	C_{root}	Root chord	5 m
	C_{tip}	Tip chord	1.5 m
	S	Planform area (single wing)	45.5 m^2
	MAC	Mean aerodynamic chord	3.25 m
Fuelburn calculation parameters			
	R	Nominal range	3815 km
	R_{climb}	Climb segment range	290 km
	V_{climb}	Average climb speed	350mph
	$C_{D,\text{frame}}$	Airframe drag coefficient (fuselage + tail + nacelle)	0.0152[b]
	k_{tank}	Assumed fraction of wingbox that can store fuel	0.85
	TSFC	Thrust specific fuel consumption	18×10^{-6} kg N^{-1} s[c]
	ρ_{fuel}	Fuel density	804 kg m^{-3}

[a] Approximated based on true empty weight of 31.1×10^3 kg.
[b] Computed using a conceptual design drag build-up
[c] Publicly available value for the Rolls-Royce BR700, a close relative of the 717's BR715 engine

[10] We increased the number of ribs in this geometry compared with the version available in the MPhys repository in anticipation of the optimizer increasing the wing's span

Table 3: Flight conditions

Flight point	Altitude	Mach Number	Load factor	Aircraft mass
Cruise	10 400 m	0.77	1	$\sqrt{M_{\text{cruise, start}} \times LGM}$
Maneuver	0 m	0.458	2.5	LGM

Table 4: Composite ply properties

Property	Description	Value
E_{11}	Fiber direction modulus	117.7 GPa
E_{22}	Transverse modulus	9.7 GPa
G_{12}	In-plane shear modulus	4.8 GPa
G_{13}	Transverse shear modulus	4.8 GPa
G_{23}	Transverse shear modulus	4.8 GPa
T_1	Fiber direction tensile strength	1648 MPa
C_1	Fiber direction compressive strength	1034 MPa
T_2	Transverse tensilse strength	64 MPa
C_2	Transverse compressive strength	228 MPa
S_{12}	Shear strength	71 MPa
ν_{12}	Major Poisson's ratio	0.35
ρ	Density	1550 kg m^{-3}

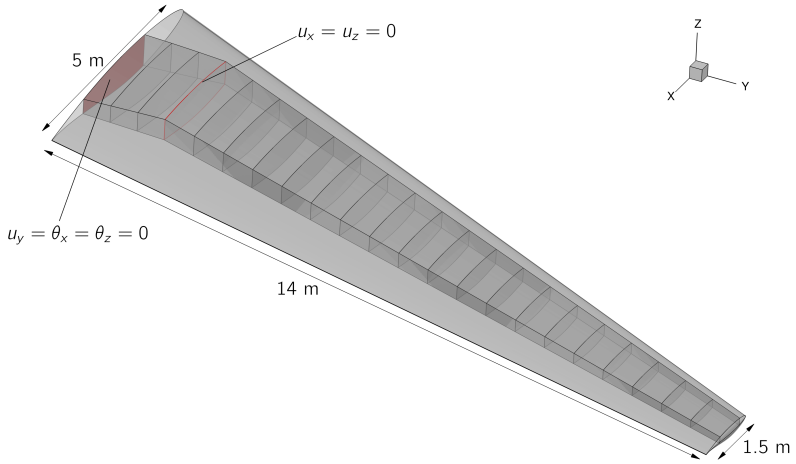

Figure 5: MACH tutorial wing OML and wingbox geometries; boundary conditions are applied to the wingbox at the side-of-body junction and symmetry plane.

4.2 Optimization Problem

4.2.1 Objective

The objective function used in all of our optimizations is the fuel-burn of the aircraft over a given mission. We compute the fuel-burn using a two-stage process that accounts for the fuel-burn in both cruise and climb. Adler and Martins [86] showed that this type of approach can be used to achieve results with similar accuracy to a full mission analysis, but with a significant reduction in computational cost. Our process starts by computing the landing gross mass (LGM) of the aircraft:

$$\text{LGM} = M_{\text{payload}} + M_{\text{frame}} + M_{\text{fuel, res}} + 2M_{\text{wing}} \tag{28}$$

The total mass of a single wing is computed using the regression model created by Elham [87]:

$$M_{\text{wing}} = 10.147 M_{\text{wingbox}}^{0.8162} \tag{29}$$

Where M_{wingbox} is the mass of the wingbox computed by TACS. Assuming the fuel-burn during descent and landing is negligible, we compute the mass at the start of the cruise phase, and then the takeoff gross mass (TOGM) by rearranging the Breguet range equation:

$$M_{\text{cruise, start}} = \text{LGM} \exp\left(\frac{R \times TSFC}{V_{\text{cruise}}}\left(\frac{D_{\text{cruise}}}{L_{\text{cruise}}}\right)\right) \tag{30}$$

$$\text{TOGM} = M_{\text{cruise, start}} \exp\left(\frac{R_{\text{climb}} \times TSFC}{V_{\text{climb}}}\left(\frac{\cos(\gamma)}{L_{\text{cruise}}/D_{\text{cruise}}} + \sin(\gamma)\right)\right) \tag{31}$$

$$FB = \text{TOGM} - \text{LGM} \tag{32}$$

Where γ is the climb angle, here computed based on the assumed climb range and cruise altitude. The lift and drag in the cruise condition are computed using a coupled aerostructural analysis in MPhys, the values are doubled to get the full aircraft values, and the drag of un-modeled components (fuselage, tail, and nacelles) is added:

$$L_{\text{cruise}} = 2L_{\text{wing}} \qquad D_{\text{cruise}} = 2\left(D_{\text{wing}} + \frac{1}{2} q_{\text{cruise}} S C_{D,\text{frame}}\right) \tag{33}$$

Where $C_{D,\text{frame}}$ is estimated using a conceptual drag build-up implemented by Adler and Martins [88] based on the methods of Torenbeek [89] and Raymer [90]. The area used in the above equation is the planform area of the baseline geometry and does not vary during optimization since we assume that the remainder of the aircraft remains identical. The assumption that the L/D in climb is the same as in cruise means our approach is less accurate than the calculation used by Adler and Martins [86], but avoids the need for an additional high-fidelity aerostructural analysis.

4.2.2 Design Variables

To allow the optimizer to trade-off between the aerodynamic and structural performance of the wing, we use a total of 576 structural sizing and geometric design variables, these variables are summarized in Figure 6 and Tables 5 and 6. Figure 6a shows the OML and wingbox inside the FFD control volume that paramterizes the geometry. The FFD consists of 6 sections, each with 8 points in the chordwise direction close to the upper and lower surfaces of the wing. These 96 control points can be moved vertically to change the shape of each wing section and each section except the root can be rotated to change the twist distribution. To alter the wing's planform, the optimizer can vary the root and tip chord lengths, and move the wing tip in the spanwise and chordwise directions to change span and sweep.

Figures 6b and 6c show the structural parameterization of the wingbox. We treat each rib, and each skin and spar segment between a pair of ribs as a separate panel and parameterize them with the 4 variables shown in Figure 6c describing a stiffened shell with T-shape stiffeners. The stiffener flange fraction, k_f, is set at 1 for all panels. An additional panel length variable does not affect the stiffness or geometry of the wingbox but must be passed to each element to compute the buckling failure criteria described in Section 2.4. We add a set of constraints to ensure that the panel length design variables are consistent with the true length of each panel.

Finally, the optimizer can also control the angles of attack at the cruise and maneuver flight points to meet the lift constraints described in Section 4.2.3.

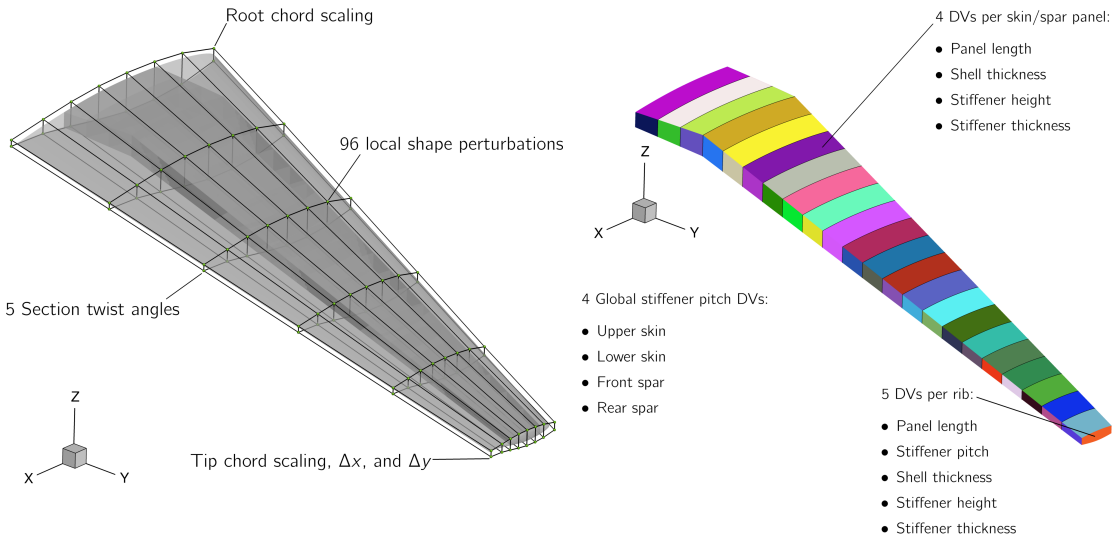

(a) Geometric variables control the cross-sections, twist distribution, and planform of the wing

(b) Structural variables control the sizing of each wingbox panel

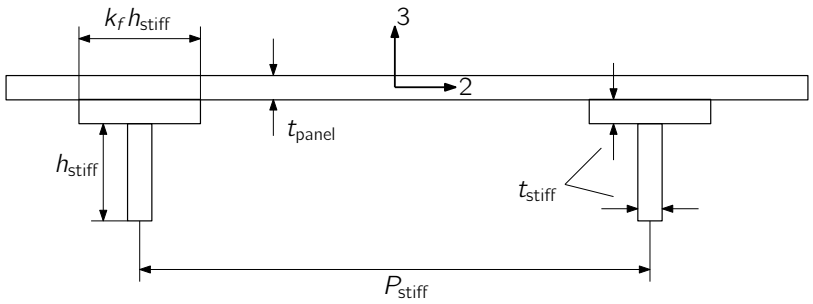

(c) Each wingbox panel is parameterized by multiple sizing variables for the shell and stiffener

Figure 6: We parameterize both the geometry and structural sizing of the wing using 578 design variables

Table 5: The design variables in our optimization problem give the optimizer detailed control over both the wing's geometry and structural sizing.

Variable	Description	Quantity	Bounds
θ	Twist	5	$[-15, 15]$ °
x_{chord}	Chord scaling	2	$[0.5, 2]$
x_{span}	Span change	1	$[-10, 20]$ m
x_{sweep}	Tip shear	1	$[-5, 5]$ m
x_{shape}	Local shape	96	$[-0.5, 0.5]$ m
$\alpha_{cruise}, \alpha_{man}$	Cruise and maneuver angle of attack	2	$[-10, 20]$ °
x_{struct}	Structural sizing[a]	471	
	Total	**578**	

[a] See Table 6 for details.

Table 6: Structural sizing variable breakdown

Variable	Description	Lower skin	Upper skin	Spars	Ribs	Quantity	Bounds
$\tilde{L}_{\text{panel}}$	Panel length	✓	✓	✓	✓	111	$[0, \infty]$
t_{panel}	Panel thickness	✓	✓	✓	✓	111	$[2, 100]$ mm
t_{stiff}	Stiffener thickness	✓	✓	✓	✓	111	$[2, 100]$ mm
h_{stiff}	Local stiffener height	✓	✓	✓	✓	111	$[2, 100]$ mm
h_{stiff}	Local stiffener pitch				✓	23	$[50, 500]$ mm
p_{stiff}	Global stiffener pitch	✓	✓	✓		4	$[50, 500]$ mm
					Total	**471**	

4.2.3 Constraints

Table 7 summarizes the 1287 constraints applied in our optimizations. The strength ratios in all elements of the wingbox model in the maneuver flight point are KS-aggregated into four constraint values, one each for the ribs, spars, upper skin, and lower skin. These values are constrained to lie below $1/1.5$ so that the wingbox has a safety factor of 1.5. We constrain the lift produced by the wing at each flight point to equal the weight of the aircraft multiplied by the relevant load factor. We model the maneuver condition at the landing gross mass since the inertial relief of the fuel is not included in our structural model. The aircraft mass for the cruise condition is taken to be the mid-cruise mass, which we compute using a geometric average of the mass at the start and end of the cruise segment to account for the non-uniform rate of fuel burn over the segment.

Since we only consider two flight points, additional constraints are required to ensure the optimizer produces a realistic wing geometry, these are shown in Figure 7. To maintain reasonable low-speed performance, we enforce that the leading edge radius of the wing remains at least 90% of the baseline value at 20 points along the span, we also compute the projected planform area of the wing and use it to enforce a maximum allowable wing loading (TOGM/$2S$) of $650\,\text{kg}\,\text{m}^{-2}$. We compute the volume of the wingbox and enforce that it is large enough to store the fuel required for the mission, assuming that fuel tanks make up 85% of the wingbox. The height of the front and rear spars at 20 points along the span is constrained to be at least 75% its original value to maintain the space required to mount components such as control surface actuators [91]. Finally, the region between the rear spar and the trailing edge is constrained to maintain at least 50% of its original thickness to prevent the optimizer create an unrealistically thin trailing edge, which is a common issue in aerodynamic shape optimization.

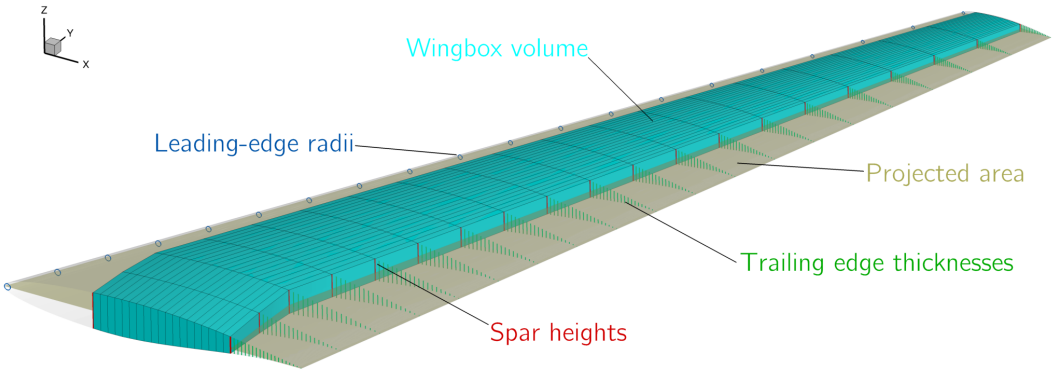

Figure 7: We enforce a series of constraints to ensure the optimization produces a realistic geometry.

To avoid abrupt changes in panel sizing we enforce adjacency constraints. The change in panel and stiffener thicknesses between adjacent skin and spar panels is limited to 2.5 mm and the change in stiffener height to 10 mm. We also enforce some basic structural sizing rules on all panels, the aspect-ratio of the stiffener web ($h_{\text{stiff}}/t_{\text{stiff}}$) is constrained to be between 2 and 10, and the difference between the panel and stiffener thicknesses is limited to 2.5 mm. These constraints, although numerous, are linear and are handled efficiently by SNOPT, without the need for repeated gradient calculations.

Table 7: Nonlinear and linear constraints applied in the optimization problem

Function	Description	Quantity	
		Nonlinear	**Linear**
$1.5KS_{SR} \leq 1$	Maneuver strength ratios	4	
$L_{\text{cruise}} = M_{\text{cruise, mid}}g$	Mid-cruise lift level	1	
$L_{\text{cruise}} = 2.5LGMg$	Maneuver lift level	1	
$t_{\text{spar}} \geq 0.75t_{\text{spar},0}$	Spar height	40	
$t \geq t_0/2$	TE thickness	400	
$R_{\text{LE}} \geq 0.9R_{\text{LE},0}$	Leading edge radius	20	
$V_{\text{fuel}} \leq V_{\text{tank}}$	Fuel volume	1	
$TOGM/2S \leq 650\,\text{kg m}^{-2}$	Maximum wing loading	1	
$\tilde{L}_{\text{panel},i} = L_{\text{panel},i}$	Panel length consistency	111	
$\left\lvert t_{\text{panel},i} = t_{\text{panel},j} \right\rvert \leq 2.5\,\text{mm}$	Skin/spar panel thickness adjacency		84
$\left\lvert t_{\text{stiff},i} = t_{\text{stiff},j} \right\rvert \leq 2.5\,\text{mm}$	Skin/spar stiffener thickness adjacency		84
$\left\lvert h_{\text{stiff},i} = h_{\text{stiff},j} \right\rvert \leq 10\,\text{mm}$	Skin/spar stiffener height adjacency		84
$\left\lvert t_{\text{panel},i} = t_{\text{stiff},i} \right\rvert \leq 2.5\,\text{mm}$	Panel-stiffener thickness difference		111
$h_{\text{stiff},i} \leq 10t_{\text{stiff},i}$	Maximum stiffener aspect-ratio		111
$h_{\text{stiff},i} \geq 2t_{\text{stiff},i}$	Minimum stiffener aspect-ratio		111
$2h_{\text{stiff},i} \leq p_{\text{stiff},i}$	Minimum stiffener spacing		111
$x_{\text{shape},i} = -x_{\text{shape},j}$	FFD leading/traing-edge constraints		12
	Total	**579**	**708**

5 Results

In this section, we compare the results of our aerostructural optimization using both linear and nonlinear structural models. To do this, we first optimize the wing with a fixed planform, removing the span, sweep and chord design variables. Then, starting from this baseline, we optimize the wing including the planform variables, both for the original Boeing 717 range of 3815 km and also for a 50% extended range of 5722 km. We repeat this process using linear and nonlinear structural models.

Each optimization runs using the coarse CFD and FE meshes on 36 Intel Xeon Gold 6154 processor cores for 2 days. In this period, the optimizer achieves our desired feasibility of 10^{-6} but fails to reach our desired optimality of 10^{-6}. The optimality instead stalls around 10^{-4}, a reduction of three orders of magnitude from the initial point. This stalling is likely due to limitations in the accuracy of the coupled aerostructural derivatives due the poor conditioning of the structural model, as noted by Kenway et al. [5].

Figure 9 shows the planform geometry and equivalent axial thickness[11] distributions for each set

[11] The equivalent axial thickness is the thickness of an unstiffened shell with the same cross-section area as the stiffened panel.

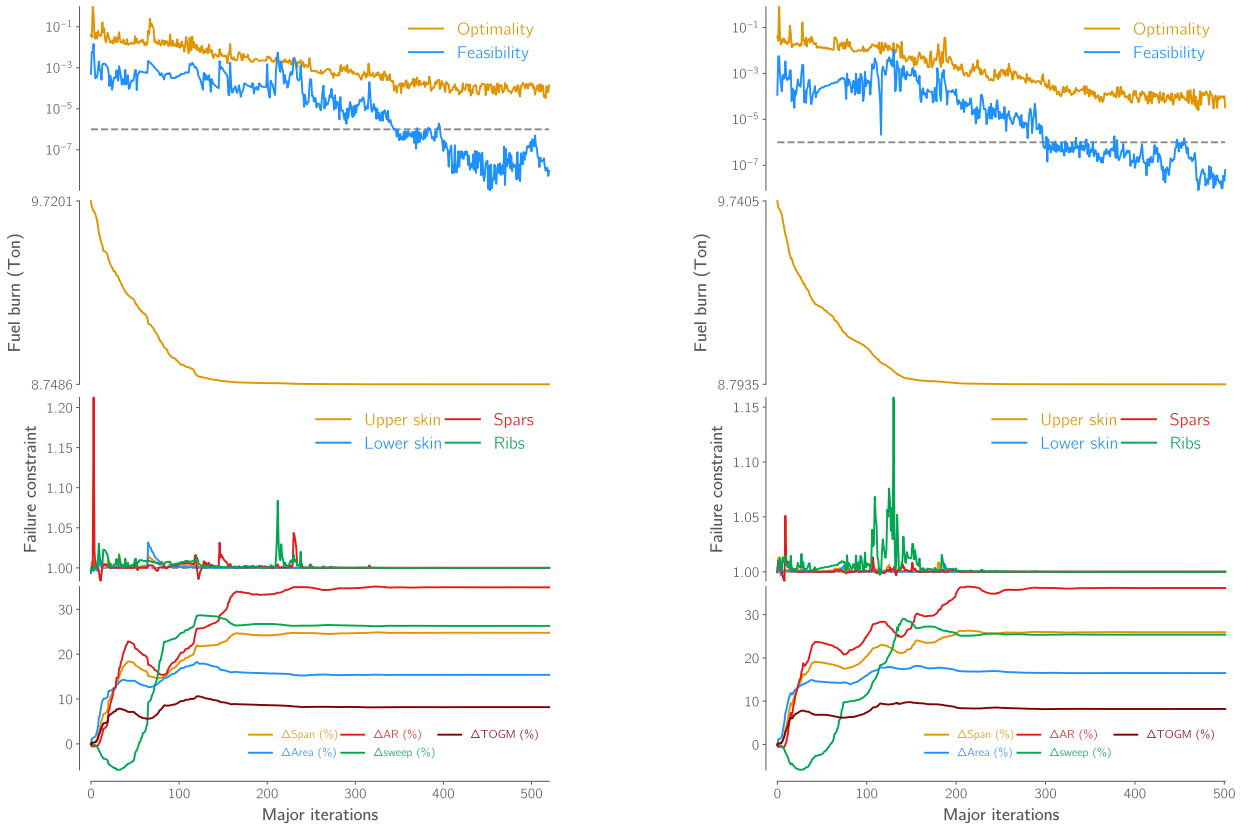

(a) Linear structural model

(b) Nonlinear structural model

Figure 8: Optimization histories for the two nominal range fuel-burn minimization cases including planform variables. Both cases are well converged but cannot reach the target optimality due to poor conditioning.

of optimized wings. Compared to the fixed planform case, the optimizer significantly increases the aspect-ratio of the wing to reduce induced drag when given the freedom to do so. The optimizer also increases the backward sweep of the wing, likely to increase the bend-twist coupling of the wing, which results in passive load alleviation in the maneuver condition.

For a more quantitative view of the same data, Figure 10 shows the trends for numerous quantities of interest vs range for the three cases. The optimized fuel-burn values with the linear and nonlinear structural models are within 1% of each other. The fuel-burn is always higher when using the nonlinear structural model, likely due to the shortening of the effective wing span caused by the geometrically nonlinear bending kinematics. However, some of the design trends between the nominal and extended range cases do differ depending on the structural model. The optimized aspect-ratio for the nominal mission range is 12.45, a 44% increase over the baseline planform. Moving from the nominal to the extended range design, the optimum aspect ratio decreases by approximately 10%, to 11.2 and 11.02 for the linear and nonlinear cases respectively. In the nonlinear cases, the semispan of the wing remains roughly constant during this change and the aspect ratio decreases due to an increase in the wing's chord. In the linear case, the chord increase is accompanied by a span increase, which results in the marginally higher aspect-ratio and lift-to-drag ratio. The wing mass, however, increases by 10% when moving from the nominal to the extended range case. This is in contrast to the cases using the nonlinear structural model, where the wing mass decreases by 4%. These trends suggest that at this point in the design space, the structural mass penalty for a unit increase in the span

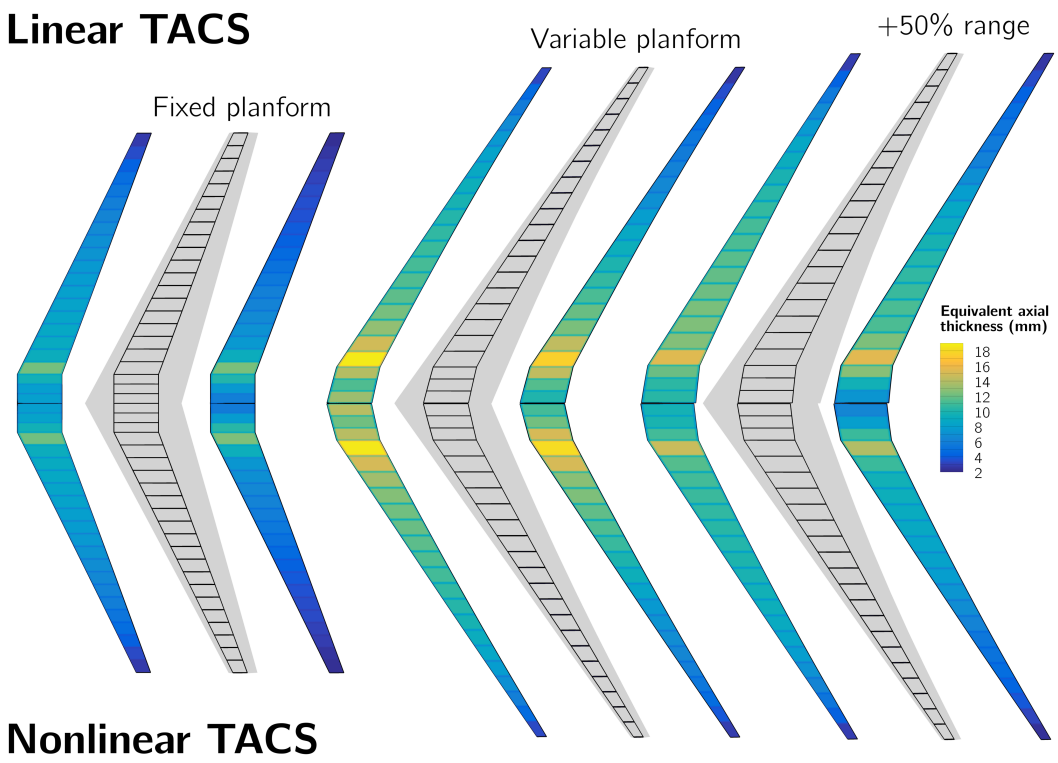

Figure 9: Optimized wing designs for the fixed planform, variable planform, and 50% extended range cases. The thickness distributions of the upper and lower skins of the wingbox are shown to the left and right of each wing, respectively. The optimizer significantly increases the aspect-ratio of the wing when given the freedom, but the optimum wing planform does not change significantly when the range is extended or when a nonlinear structural model is used.

is significantly higher when using the nonlinear structural model, and the optimizer thus focuses on decreasing structural mass as the range is extended rather than minimizing drag.

One quantity that is consistently higher when using a nonlinear structural model is the mass of the wingbox ribs. In the extended range case, the mass of the ribs is 5% higher when using a nonlinear structural model, even though the total wing mass is 11% lower. This is because the nonlinear model captures the rib-crushing loads that occur due to the bending deformation of the wingbox. These crushing loads force the optimizer to reinforce the ribs to satisfy the buckling constraint, resulting in a more realistically sized wingbox. Figure 11 demonstrates this by comparing the equivalent bending thickness[12] of the ribs in the optimized wingboxes from the extended range cases. The differences in rib sizing are most pronounced in the root region of the wing, where the bending moments are highest. Despite the consistency of this effect, its impact on the overall design of the wing is likely negligible given that the ribs make up less than 2% of the total mass of the aircraft.

6 Conclusions

If MDO is to be successfully applied to the design of commercial aircraft, it needs to be able to account for the geometrically nonlinear aeroelastic effects caused by their increasing in-flight deformations. In this work, we presented our implementation of efficient and robust methods for geometrically nonlinear

[12] The equivalent bending thickness is the thickness of an unstiffened shell with the same bending stiffness as the stiffened panel.

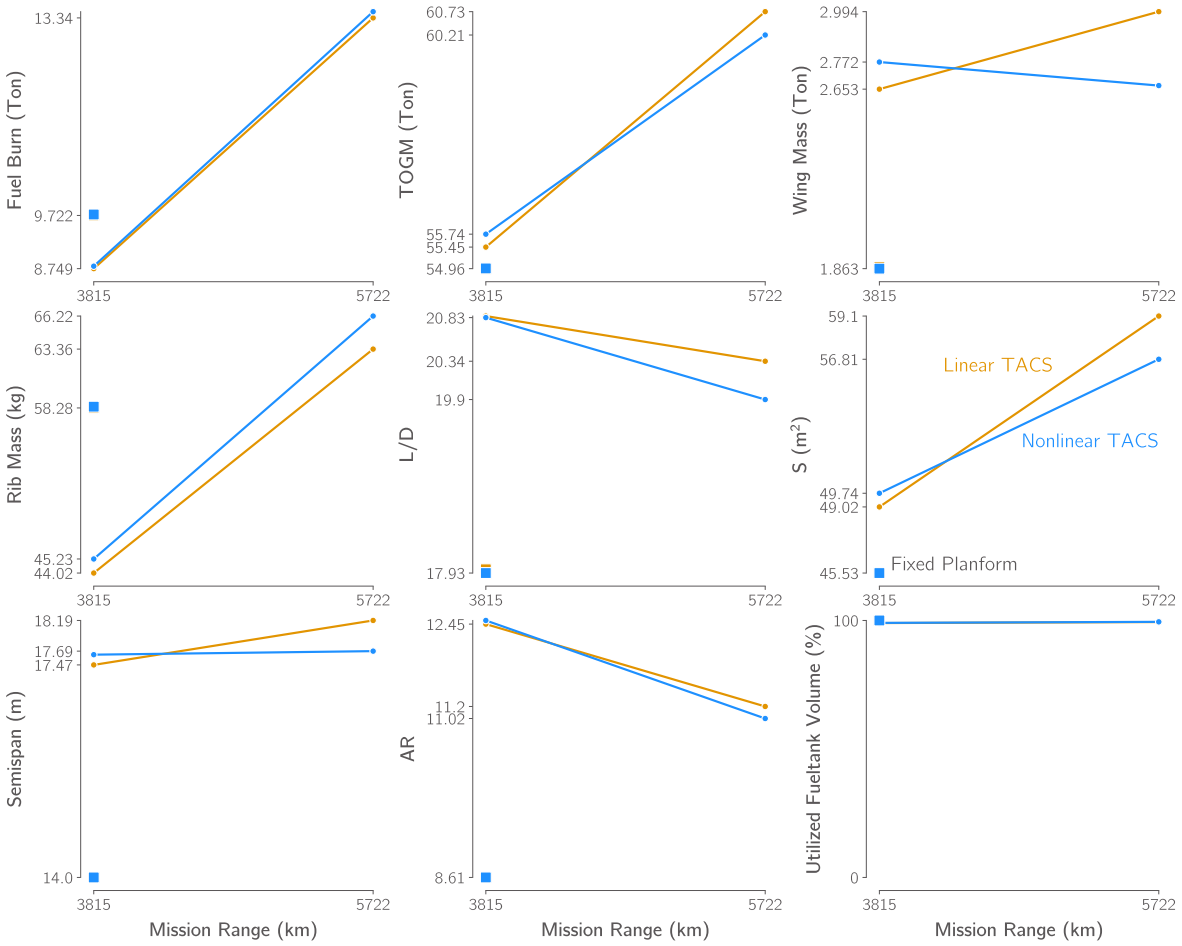

Figure 10: Although the fuel-burn of the wings optimized with linear and nonlinear structural models are within 1% of each other, other quantities like the wing mass differ by as much as 10%. This suggests that geometrically nonlinear phenomena may have significant effects on the trade-off between structural mass and induced drag.

analysis and optimization of realistic aerospace shell structures in the finite element code TACS. The implementation includes a novel geometrically nonlinear shell element formulation that uses a quadratic rotation parameterization to capture the moderate rotations seen in the wings of very flexible aircraft. To solve the resulting nonlinear residual equations, we implement a nonlinear static structural solver that uses a predictor-corrector continuation method, adaptive linear convergence, and an energy minimization method for restarting analyses from previous solutions.

Using the existing interface between TACS and the multiphysics coupling library MPhys, we demonstrated what we believe to be the first simultaneous optimization of a wing's aerodynamic shape and structural sizing using high-fidelity geometrically nonlinear models. Our optimization problem aimed to minimize the fuel-burn of a wing based on that of a Boeing 717, by varying 578 design variables, subject to 1287 constraints on material failure, geometric properties, and structural sizing rules. In all the results we presented, the optimal fuel-burn was not greatly affected by the use of a geometrically nonlinear structural model. However, other quantities of interest, such as the optimized wing mass, were significantly affected. The result of our extended range optimization cases suggests that the inclusion of geometrically nonlinear effects incentivized the optimizer more towards reducing structural mass than reducing drag as they resulted in a 10% lighter, but also less aerodynamically efficient

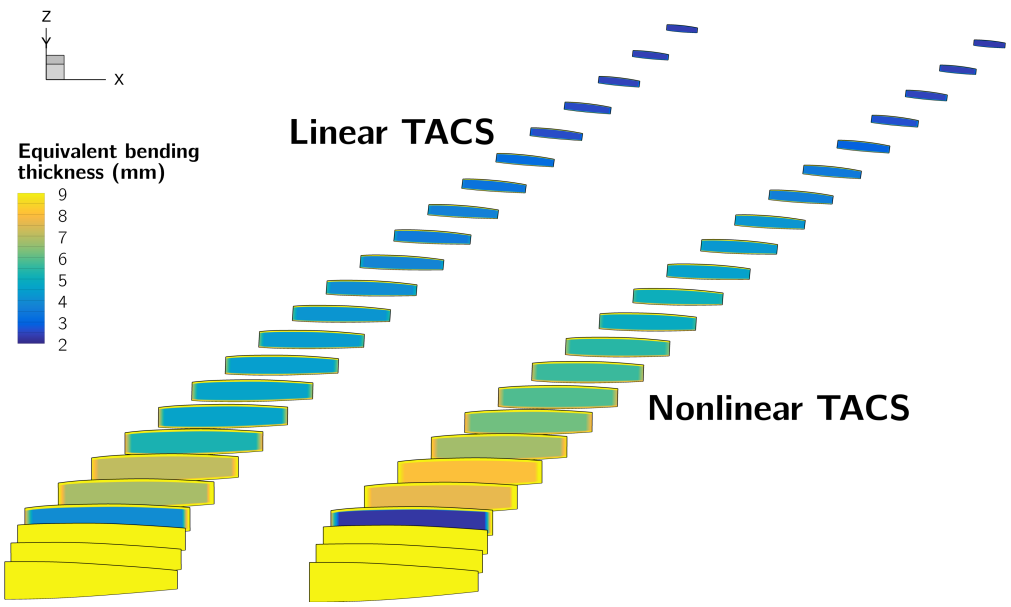

Figure 11: Rib crushing loads captured by the nonlinear structural model necessitate ribs with higher bending stiffness, particularly near the side-of-body junction.

wing. Although the aspect-ratios at which geometrically nonlinear effects are seen in this work are significantly higher than the baseline design, they are not significantly higher than those of the latest generation of commercial aircraft such as the Boeing 787.

Despite these encouraging results, it would certainly not be wise to draw definitive conclusions from the limited set of data presented in this work. Our future work will focus on running optimizations with finer CFD meshes, which has the potential to change the trade-off between structural mass and drag and thus any planform design trends seen in this work. We are also working on a more comprehensive exploration of the mission parameter space. Conducting optimizations over a more comprehensive set of mission ranges and aircraft sizes, we hope to better understand the kinds of aircraft for which geometric nonlinearity is most consequential.

Acknowledgments

The authors would like to thank Timothy Brooks for his extensive development work on the Python and MPhys interfaces for TACS, which made this work possible. This research was supported in part through computational resources and services provided by Advanced Research Computing at the University of Michigan, Ann Arbor. This work also used the stampede2 cluster at the Texas Advanced Computing Center through allocation TG-DDM140001 from the Advanced Cyberinfrastructure Coordination Ecosystem: Services & Support (ACCESS) program, which is supported by National Science Foundation grants #2138259, #2138286, #2138307, #2137603, and #2138296

References

[1] Castellani, M., Cooper, J. E., and Lemmens, Y., "Nonlinear static aeroelasticity of high-aspect-ratio-wing aircraft by finite element and multibody methods," *Journal of Aircraft*, Vol. 54, No. 2, 2017, pp. 548–560. doi:10.2514/1.C033825.

[2] Brooks, T. R., Martins, J. R. R. A., and Kennedy, G. J., "Aerostructural Trade-offs for Tow-steered Composite Wings," *Journal of Aircraft*, Vol. 57, No. 5, 2020, pp. 787–799. doi:10.2514/1.C035699.

[3] Brooks, T. R., Kenway, G. K. W., and Martins, J. R. R. A., "Benchmark Aerostructural Models for the Study of Transonic Aircraft Wings," *AIAA Journal*, Vol. 56, No. 7, 2018, pp. 2840–2855. doi:10.2514/1.J056603.

[4] Kenway, G. K. W., and Martins, J. R. R. A., "Multipoint High-Fidelity Aerostructural Optimization of a Transport Aircraft Configuration," *Journal of Aircraft*, Vol. 51, No. 1, 2014, pp. 144–160. doi:10.2514/1.C032150.

[5] Kenway, G. K. W., Kennedy, G. J., and Martins, J. R. R. A., "Scalable Parallel Approach for High-Fidelity Steady-State Aeroelastic Analysis and Adjoint Derivative Computations," *AIAA Journal*, Vol. 52, No. 5, 2014, pp. 935–951. doi:10.2514/1.J052255.

[6] Brazier, L. G., "On the Flexure of Thin Cylindrical Shells and Other "Thin" Sections," *Proceedings of the Royal Society A: Mathematical, Physical and Engineering Sciences*, Vol. 116, No. 773, 1927, pp. 104–114. doi:10.1098/rspa.1927.0125.

[7] Stanford, B. K., and Dunning, P. D., "Optimal Topology of Aircraft Rib and Spar Structures Under Aeroelastic Loads," *Journal of Aircraft*, Vol. 52, No. 4, 2015, pp. 1298–1311. doi:10.2514/1.C032913.

[8] Gray, A. C., and Martins, J. R. R. A., "Geometrically Nonlinear High-fidelity Aerostructural Optimization for Highly Flexible Wings," *Proceedings of the AIAA SciTech Forum*, 2021. doi:10.2514/6.2021-0283.

[9] Howcroft, C., Cook, R., Calderon, D., Lambert, L., Castellani, M., Cooper, J. E., Lowenberg, M. H., and Neild, S., "Aeroelastic modelling of highly flexible wings," *15th Dynamics Specialists Conference*, AIAA, San Diego, 2016. doi:10.2514/6.2016-1798.

[10] Garcia, J. A., "Numerical investigation of nonlinear aeroelastic effects on flexible high-aspect-ratio wings," *Journal of Aircraft*, Vol. 42, No. 4, 2005, pp. 1025–1036. doi:10.2514/1.6544.

[11] Gray, A. C., Riso, C., Jonsson, E., Martins, J. R. R. A., and Cesnik, C. E. S., "High-fidelity Aerostructural Optimization with a Geometrically Nonlinear Flutter Constraint," *International Forum on Aeroelasticity and Structural Dynamics (IFASD 2022)*, Madrid, Spain, 2022.

[12] Dowell, E., Edwards, J., and Strganac, T. W., "Nonlinear aeroelasticity," *Collection of Technical Papers - AIAA/ASME/ASCE/AHS/ASC Structures, Structural Dynamics and Materials Conference*, Vol. 5, No. 5, 2003, pp. 3824–3847. doi:10.2514/2.6876.

[13] Patil, M. J., and Hodges, D. H., "On the importance of aerodynamic and structural geometrical nonlinearities in aeroelastic behavior of high-aspect-ratio wings," *Journal of Fluids and Structures*, Vol. 19, No. 7, 2004, pp. 905–915. doi:10.1016/j.jfluidstructs.2004.04.012.

[14] Su, W., "Coupled Nonlinear Aeroelasticity and Flight Dynamics of Fully Flexible Aircraft," Phd, University of Michigan, 2008. doi:10.1007/s13398-014-0173-7.2.

[15] Cavagna, L., Ricci, S., and Riccobene, L., "Structural sizing, aeroelastic analysis, and optimization in aircraft conceptual design," *Journal of Aircraft*, Vol. 48, No. 6, 2011, pp. 1840–1855. doi:10.2514/1.C031072.

[16] Harmin, M. Y., and Cooper, J. E., "Aeroelastic behaviour of a wing including geometric nonlinearities," *Aeronautical Journal*, Vol. 115, No. 1174, 2011, pp. 767–777. doi:10.1017/S0001924000006515.

[17] Palacios, R., Wang, Y., Wynn, A., and Karpel, M., "Condensation of large finite-element models for wing load analysis with geometrically-nonlinear effects," *IFASD 2013 - International Forum on Aeroelasticity and Structural Dynamics*, 2013, pp. 1–25.

[18] Bartels, R. E., Scott, R. C., Allen, T. J., and Sexton, B. W., "Aeroelastic analysis of SUGAR truss-braced wing wind-tunnel model using FUN3D and a nonlinear structural model," *56th AIAA/ASCE/AHS/ASC Structures, Structural Dynamics, and Materials Conference*, 2015. doi:10.2514/6.2015-1174.

[19] Castellani, M., Cooper, J. E., and Lemmens, Y., "Nonlinear static aeroelasticity of high-aspect-ratio-wing aircraft by finite element and multibody methods," *Journal of Aircraft*, Vol. 54, No. 2, 2017, pp. 548–560. doi:10.2514/1.C033825.

[20] Ritter, M., Teixeira, P. C., and Cesnik, C. E., "Comparison of nonlinear aeroelastic methods for maneuver simulation of very flexible aircraft," *AIAA/ASCE/AHS/ASC Structures, Structural Dynamics, and Materials Conference, 2018*, 2018. doi:10.2514/6.2018-1953.

[21] Riso, C., Di Vincenzo, F. G., Ritter, M., Cesnik, C. E., and Mastroddi, F., "Nonlinear aeroelastic trim of very flexible aircraft described by detailed models," *Journal of Aircraft*, Vol. 55, No. 6, 2018, pp. 2338–2346. doi:10.2514/1.C034787.

[22] Lupp, C. A., and Cesnik, C. E. S., "A Gradient-Based Flutter Constraint Including Geometrically Nonlinear Deformations," *2019 AIAA/ASCE/AHS/ASC Structures, Structural Dynamics, and Materials Conference*, AIAA, San Diego, California, 2019.

[23] Medeiros, R. R., Cesnik, C. E. S., and Coetzee, E. B., "Computational Aeroelasticity Using Modal-Based Structural Nonlinear Analysis," *AIAA Journal*, 2019, pp. 1–10. doi:10.2514/1.j058593.

[24] Verri, A. A., Bussamra, F. L., de Morais, K. C., Becker, G. G., Cesnik, C. E., Luque Filho, G. B., and de Oliveira, L. C., "Static loads evaluation in a flexible aircraft using high-fidelity fluid–structure iteration tool (E2-FSI): extended version," *Journal of the Brazilian Society of Mechanical Sciences and Engineering*, Vol. 42, No. 1, 2020. doi:10.1007/s40430-019-2154-4.

[25] Zimmer, M., Feldwisch, J. M., and Ritter, M., "Coupled CFD-CSM Analyses of a Highly Flexible Transport Aircraft by Means of Geometrically Nonlinear Methods," *International Forum on Aeroelasticity and Structural Dynamics (IFASD 2022)*, Madrid, 2022.

[26] Calderon, D. E., Cooper, J. E., Lowenberg, M. H., and Neild, S. A., "On the Effect of Including Geometric Nonlinearity in the Sizing of a Wing," *AIAA/ASCE/AHS/ASC Structures, Structural Dynamics, and Materials Conference, 2018*, Kissimmee, 2018. doi:10.2514/6.2018-1680.

[27] Calderon, D. E., Cooper, J. E., Lowenberg, M., Neild, S. A., and Coetzee, E. B., "Sizing High-Aspect-Ratio Wings with a Geometrically Nonlinear Beam Model," *Journal of Aircraft*, Vol. 56, No. 4, 2019, pp. 1455–1470. doi:10.2514/1.c035296.

[28] Werter, N. P., and De Breuker, R., "A novel dynamic aeroelastic framework for aeroelastic tailoring and structural optimisation," *Composite Structures*, Vol. 158, 2016, pp. 369–386. doi:

10.1016/j.compstruct.2016.09.044, URL http://dx.doi.org/10.1016/j.compstruct.2016.09.044.

[29] Krüger, W. R., Dillinger, J., De Breuker, R., and Haydn, K., "Investigations of passive wing technologies for load reduction," *CEAS Aeronautical Journal*, Vol. 10, No. 4, 2019, pp. 977–993. doi:10.1007/s13272-019-00393-2, URL https://doi.org/10.1007/s13272-019-00393-2.

[30] Lancelot, P., and De Breuker, R., "Transonic Flight and Movable Load Modelling for Wing-Box Preliminary Sizing," *18th International Forum on Aeroelasticity and Structural Dynamics*, , No. June, 2019, pp. 28–30.

[31] Rajpal, D., Gillebaart, E., and De Breuker, R., "Preliminary aeroelastic design of composite wings subjected to critical gust loads," *Aerospace Science and Technology*, Vol. 85, 2019, pp. 96–112. doi:10.1016/j.ast.2018.11.051, URL https://doi.org/10.1016/j.ast.2018.11.051.

[32] Rajpal, D., Kassapoglou, C., and De Breuker, R., "Aeroelastic optimization of composite wings including fatigue loading requirements," *Composite Structures*, Vol. 227, No. August, 2019, p. 111248. doi:10.1016/j.compstruct.2019.111248, URL https://doi.org/10.1016/j.compstruct.2019.111248.

[33] Natella, M., and De Breuker, R., "The effects of a full-aircraft aerodynamic model on the design of a tailored composite wing," *CEAS Aeronautical Journal*, Vol. 10, No. 4, 2019, pp. 995–1014. doi:10.1007/s13272-019-00366-5, URL http://dx.doi.org/10.1007/s13272-019-00366-5.

[34] Bordogna, M. T., Lancelot, P., Bettebghor, D., and De Breuker, R., "Aeroelastic tailoring for static and dynamic loads with blending constraints," *17th International Forum on Aeroelasticity and Structural Dynamics, IFASD 2017*, Vol. 2017-June, No. June, 2017.

[35] Jovanov, K., "High-Fidelity Load and Gradient Corrections for Static Aeroelastic Tailoring of Composite Wings," Phd, TU Delft, 2019. doi:10.4233/uuid, URL https://doi.org/10.4233/uuid:14b55d5e-586a-4641-8990-55a397674db8.

[36] Stanford, B., Wieseman, C. D., and Jutte, C., "Aeroelastic Tailoring of Transport Wings Including Transonic Flutter Constraints," *56th AIAA/ASCE/AHS/ASC Structures, Structural Dynamics, and Materials Conference*, Kissimmee, FL, 2015. doi:10.2514/6.2015-1127.

[37] Stanford, B., "Aeroservoelastic Optimization of a Transport Aircraft Wingbox under Stochastic Gust Constraints," *Journal of Aeroelasticity and Structural Dynamics*, Vol. 6, No. 1, 2018, pp. 21–41. doi:10.3293/asdj.2018.48.

[38] Stanford, B. K., "Aeroelastic Wingbox Stiffener Topology Optimization," *Journal of Aircraft*, Vol. 55, No. 3, 2017, pp. 1244–1251. doi:10.2514/1.C034653.

[39] Stanford, B. K., Jutte, C. V., and Coker, C. A., "Aeroelastic Sizing and Layout Design of a Wingbox Through Nested Optimization," *AIAA Journal*, Vol. 57, No. 2, 2018, pp. 848–857. doi:10.2514/1.j057428.

[40] Stanford, B. K., and Dunning, P. D., "Optimal Topology of Aircraft Rib and Spar Structures Under Aeroelastic Loads," *Journal of Aircraft*, Vol. 52, No. 4, 2014, pp. 1298–1311. doi:10.2514/1.C032913.

[41] Stanford, B. K., "Shape , Sizing , and Topology Design of a Wingbox under Aeroelastic Constraints," *AIAA Aviation 2020 Forum*, 2020. doi:10.2514/6.2020-3147.

[42] Dillinger, J. K., Abdalla, M. M., Meddaikar, Y. M., and Klimmek, T., "Static aeroelastic stiffness optimization of a forward swept composite wing with CFD-corrected aero loads," *CEAS Aeronautical Journal*, Vol. 10, No. 4, 2019, pp. 1015–1032. doi:10.1007/s13272-019-00397-y, URL https://doi.org/10.1007/s13272-019-00397-y.

[43] Brooks, T. R., Martins, J. R. R. A., and Kennedy, G. J., "High-fidelity Aerostructural Optimization of Tow-steered Composite Wings," *Journal of Fluids and Structures*, Vol. 88, 2019, pp. 122–147. doi:10.1016/j.jfluidstructs.2019.04.005.

[44] Burdette, D. A., and Martins, J. R. R. A., "Impact of Morphing Trailing Edge on Mission Performance for the Common Research Model," *Journal of Aircraft*, Vol. 56, No. 1, 2019, pp. 369–384. doi:10.2514/1.C034967.

[45] Kennedy, G. J., Kenway, G. K. W., and Martins, J. R. R. A., "High Aspect Ratio Wing Design: Optimal Aerostructural Tradeoffs for the Next Generation of Materials," *Proceedings of the AIAA Science and Technology Forum and Exposition (SciTech)*, National Harbor, MD, 2014. doi:10.2514/6.2014-0596.

[46] Kenway, G. W. K., and Martins, J. R. R. A., "High-fidelity aerostructural optimization considering buffet onset," *Proceedings of the 16th AIAA/ISSMO Multidisciplinary Analysis and Optimization Conference*, Dallas, TX, 2015. doi:10.2514/6.2015-2790.

[47] Su, W., and Cesnik, C. E. S., "Nonlinear Aeroelasticity of a Very Flexible Blended-Wing-Body Aircraft," *Journal of Aircraft*, Vol. 47, No. 5, 2010, pp. 1539–1553. doi:10.2514/1.47317.

[48] Bons, N. P., He, X., Mader, C. A., and Martins, J. R. R. A., "Multimodality in Aerodynamic Wing Design Optimization," *AIAA Journal*, Vol. 57, No. 3, 2019, pp. 1004–1018. doi:10.2514/1.J057294.

[49] Stickan, B., Schröder, F., Helm, S., and Bleecke, H., *On Recent Advances in Industrial High-Fidelity Aeroelasticity*, Notes on Numerical Fluid Mechanics and Multidisciplinary Design, Springer International Publishing, 2018, pp. 85–101. doi:10.1007/978-3-319-72020-3_6.

[50] Kennedy, G. J., and Martins, J. R. R. A., "A Parallel Finite-Element Framework for Large-Scale Gradient-Based Design Optimization of High-Performance Structures," *Finite Elements in Analysis and Design*, Vol. 87, 2014, pp. 56–73. doi:10.1016/j.finel.2014.04.011.

[51] Dvorkin, E. N., and Bathe, K.-J., "A continuum mechanics based four-node shell element for general nonlinear analysis," *Engineering Computations*, Vol. 1, 1984, pp. 77–88. doi:10.1108/eb023562.

[52] Bathe, K.-J., and Dvorkin, E. N., "A formulation of general shell elements – the use of mixed interpolation of tensorial components," *International Journal for Numerical Methods in Engineering*, Vol. 22, 1986, pp. 697–722. doi:10.1002/nme.1620220312.

[53] Simo, J., Fox, D., and Hughes, T., "Formulations of finite elasticity with independent rotations," *Computer Methods in Applied Mechanics and Engineering*, Vol. 95, No. 2, 1992, pp. 277 – 288. doi:10.1016/0045-7825(92)90144-9.

[54] Fox, D., and Simo, J., "A drill rotation formulation for geometrically exact shells," *Computer Methods in Applied Mechanics and Engineering*, Vol. 98, No. 3, 1992, pp. 329 – 343. doi:10.1016/0045-7825(92)90002-2.

[55] Simo, J. C., and Fox, D. D., "On stress resultant geometrically exact shell model. Part I: formulation and optimal parametrization," *Comput. Methods Appl. Mech. Eng.*, Vol. 72, 1989, pp. 267–304. doi:10.1016/0045-7825(89)90002-9.

[56] Simo, J. C., Fox, D. D., and Rifai, M. S., "On a stress resultant geometrically exact shell model. Part III: Computational aspects of the nonlinear theory," *Computer Methods in Applied Mechanics and Engineering*, Vol. 79, No. 1, 1990, pp. 21 – 70. doi:10.1016/0045-7825(90)90094-3.

[57] Beluni, P. X., and Chulya, A., "An improved automatic incremental algorithm for the efficient solution of nonlinear finite element equations," *Computers and Structures*, Vol. 26, No. 1-2, 1987, pp. 99–110. doi:10.1016/0045-7949(87)90240-9, URL https://www.sciencedirect.com/science/article/pii/0045794987902409.

[58] An, H. B., Mo, Z. Y., and Liu, X. P., "A choice of forcing terms in inexact Newton method," *Journal of Computational and Applied Mathematics*, Vol. 200, No. 1, 2007, pp. 47–60. doi:10.1016/j.cam.2005.12.030.

[59] Sze, K. Y., Liu, X. H., and Lo, S. H., "Popular benchmark problems for geometric nonlinear analysis of shells," *Finite Elements in Analysis and Design*, Vol. 40, No. 11, 2004, pp. 1551–1569. doi:10.1016/j.finel.2003.11.001.

[60] Nemeth, M. P., "A Treatise on Equivalent-Plate Stiffnesses for Stiffened Laminated-Composite Plates and Plate-Like Lattices," Tech. Rep. January, NASA, 2011. URL https://ntrs.nasa.gov/citations/20110004039.

[61] Elishakoff, I., *Handbook on Timoshenko-Ehrenfest Beam and Uflyand-Mindlin Plate Theories*, World Scientific, 2019. doi:10.1142/10890.

[62] Macquart, T., Bordogna, M. T., Lancelot, P., and De Breuker, R., "Derivation and application of blending constraints in lamination parameter space for composite optimisation," *Composite Structures*, Vol. 135, 2016, pp. 224–235. doi:10.1016/j.compstruct.2015.09.016.

[63] Tsai, S. W., and Wu, E. M., "A general theory of strength for anisotropic materials," *Journal of composite materials*, Vol. 5, No. 1, 1971, pp. 58–80.

[64] Stroud, W. J., and Agranoff, N., "Minimum-mass design of filamentary composite panels under combined loads: Design procedure based on simplified buckling equations," Tech. Rep. TN-D-8257, NASA Langley Research Center, Hampton, VA, 1976.

[65] Kreisselmeier, G., and Steinhauser, R., "Systematic Control Design by Optimizing a Vector Performance Index," *International Federation of Active Controls Symposium on Computer-Aided Design of Control Systems, Zurich, Switzerland*, 1979. doi:10.1016/S1474-6670(17)65584-8.

[66] Gray, J. S., Hwang, J. T., Martins, J. R. R. A., Moore, K. T., and Naylor, B. A., "OpenMDAO: An open-source framework for multidisciplinary design, analysis, and optimization," *Structural and Multidisciplinary Optimization*, Vol. 59, No. 4, 2019, pp. 1075–1104. doi:10.1007/s00158-019-02211-z.

[67] Hwang, J. T., and Martins, J. R. R. A., "A computational architecture for coupling heterogeneous numerical models and computing coupled derivatives," *ACM Transactions on Mathematical Software*, Vol. 44, No. 4, 2018, p. Article 37. doi:10.1145/3182393.

[68] Yildirim, A., Gray, J. S., Mader, C. A., and Martins, J. R. R. A., "Boundary Layer Ingestion

Benefit for the STARC-ABL Concept," *Journal of Aircraft*, Vol. 59, No. 4, 2022, pp. 896–911. doi:10.2514/1.C036103.

[69] Anibal, J., Mader, C. A., and Martins, J. R. R. A., "Aerodynamic shape optimization of an electric aircraft motor surface heat exchanger with conjugate heat transfer constraint," *International Journal of Heat and Mass Transfer*, Vol. 189, 2022, p. 122689. doi:10.1016/j.ijheatmasstransfer.2022.122689.

[70] Crovato, A., Boman, R., Terrapon, V. E., Dimitriadis, G., Prado, A. P., and Cabral, P. H., "Fast Full Potential Based Aerostructural Optimization Calculations For Preliminary Aircraft Design," *International Forum on Aeroelasticity and Structural Dynamics (IFASD 2022)*, Madrid, 2022, pp. 1–18.

[71] Jacobson, K. E., and Stanford, B. K., "Flutter-Constrained Optimization with the Linearized Frequency-Domain Approach," *AIAA Science and Technology Forum and Exposition, AIAA SciTech Forum 2022*, 2022. doi:10.2514/6.2022-2242.

[72] Mader, C. A., Kenway, G. K. W., Yildirim, A., and Martins, J. R. R. A., "ADflow: An open-source computational fluid dynamics solver for aerodynamic and multidisciplinary optimization," *Journal of Aerospace Information Systems*, Vol. 17, No. 9, 2020, pp. 508–527. doi:10.2514/1.I010796.

[73] Yildirim, A., Kenway, G. K. W., Mader, C. A., and Martins, J. R. R. A., "A Jacobian-free approximate Newton–Krylov startup strategy for RANS simulations," *Journal of Computational Physics*, Vol. 397, 2019, p. 108741. doi:10.1016/j.jcp.2019.06.018.

[74] Kenway, G. K. W., Mader, C. A., He, P., and Martins, J. R. R. A., "Effective Adjoint Approaches for Computational Fluid Dynamics," *Progress in Aerospace Sciences*, Vol. 110, 2019, p. 100542. doi:10.1016/j.paerosci.2019.05.002.

[75] Jacobson, K., Kiviaho, J. F., Smith, M. J., and Kennedy, G., "An Aeroelastic Coupling Framework for Time-accurate Analysis and Optimization," *2018 AIAA/ASCE/AHS/ASC Structures, Structural Dynamics, and Materials Conference*, 2018. doi:10.2514/6.2018-0100.

[76] Kiviaho, J. F., and Kennedy, G. J., "Efficient and Robust Load and Displacement Transfer Scheme Using Weighted Least Squares," *AIAA Journal*, Vol. 57, No. 5, 2019, pp. 2237–2243. doi:10.2514/1.J057318.

[77] Kenway, G. K., Kennedy, G. J., and Martins, J. R. R. A., "A CAD-Free Approach to High-Fidelity Aerostructural Optimization," *Proceedings of the 13th AIAA/ISSMO Multidisciplinary Analysis Optimization Conference*, Fort Worth, TX, 2010. doi:10.2514/6.2010-9231.

[78] Martins, J. R. R. A., and Ning, A., *Engineering Design Optimization*, Cambridge University Press, Cambridge, UK, 2021. doi:10.1017/9781108980647, URL https://mdobook.github.io.

[79] Irons, B. M., and Tuck, R. C., "A version of the Aitken accelerator for computer iteration," *International Journal for Numerical Methods in Engineering*, Vol. 1, No. 3, 1969, pp. 275–277. doi:10.1002/nme.1620010306.

[80] Saad, Y., "A Flexible Inner-Outer Preconditioned GMRES Algorithm," *SIAM Journal on Scientific Computing*, Vol. 14, No. 2, 1993, pp. 461–469. doi:10.1137/0914028.

[81] Gill, P. E., Murray, W., and Saunders, M. A., "SNOPT: An SQP Algorithm for Large-Scale Constrained Optimization," *SIAM Review*, Vol. 47, No. 1, 2005, pp. 99–131. doi:10.1137/S0036144504446096.

[82] Lyu, Z., Xu, Z., and Martins, J. R. R. A., "Benchmarking Optimization Algorithms for Wing Aerodynamic Design Optimization," *Proceedings of the 8th International Conference on Computational Fluid Dynamics*, Chengdu, Sichuan, China, 2014. ICCFD8-2014-0203.

[83] Wu, N., Kenway, G., Mader, C. A., Jasa, J., and Martins, J. R. R. A., "pyOptSparse: A Python framework for large-scale constrained nonlinear optimization of sparse systems," *Journal of Open Source Software*, Vol. 5, No. 54, 2020, p. 2564. doi:10.21105/joss.02564.

[84] Crovato, A., Prado, A. P., Cabral, P. H., Boman, R., Terrapon, V. E., and Dimitriadis, G., "A discrete adjoint full potential formulation for fast aerostructural optimization in preliminary aircraft design," *Aerospace Science and Technology*, Vol. 138, 2023, p. 108332. doi:10.1016/j.ast.2023.108332.

[85] Dillinger, J. K. S., "Static Aeroelastic Optimization of Composite Wings with Variable Stiffness Laminates," Ph.D. thesis, TU Delft, 2014. doi:10.4233/uuid:20484651-fd5d-49f2-9c56-355bc680f2b7.

[86] Adler, E. J., and Martins, J. R. R. A., "Efficient Aerostructural Wing Optimization Considering Mission Analysis," *Journal of Aircraft*, 2022. doi:10.2514/1.c037096.

[87] Mariens, J., Elham, A., and Van Tooren, M. J., "Influence of weight modelling on the outcome of wing design using multidisciplinary design optimisation techniques," *Aeronautical Journal*, Vol. 117, No. 1195, 2013, pp. 871–895. doi:10.1017/S0001924000008563.

[88] Adler, E. J., and Martins, J. R. R. A., "Blended wing body configuration for hydrogen-powered aircraft," *AIAA AVIATION Forum*, 2023.

[89] Torenbeek, E., *Synthesis of Subsonic Airplane Design*, 6th ed., Delft University Press and Kluwer Academic Publishers, 1990.

[90] Raymer, D. P., *Aircraft Design: A Conceptual Approach*, 2nd ed., AIAA, 1992.

[91] Liem, R. P., Kenway, G. K. W., and Martins, J. R. R. A., "Multimission Aircraft Fuel Burn Minimization via Multipoint Aerostructural Optimization," *AIAA Journal*, Vol. 53, No. 1, 2015, pp. 104–122. doi:10.2514/1.J052940.